QUANTUM CHEMISTRY MODELING OF HOMOGENEOUS FIRST-ROW TRANSITION METAL CATALYSIS

by

Yaqun Zhu

B.S. in Chemical Engineering & Technology, Wuhan Institute of Technology, 2009

M.Eng. in Chemical Engineering, Tianjin University, 2012

Submitted to the Graduate Faculty of

Swanson School of Engineering in partial fulfillment

of the requirements for the degree of

Master of Science

University of Pittsburgh

2015

UNIVERSITY OF PITTSBURGH

SWANSON SCHOOL OF ENGINEERING

This thesis was presented

by

Yaqun Zhu

It was defended on

July 22, 2015

and approved by

Götz Veser, Ph.D., Professor, Department of Chemical & Petroleum Engineering

Guofeng Wang, Ph.D., Assistant Professor, Department of Mechanical Engineering & Materials Science

Thesis Advisor: John A. Keith, Ph.D., Assistant Professor, Department of Chemical & Petroleum Engineering

QUANTUM CHEMISTRY MODELING OF HOMOGENEOUS FIRST-ROW

TRANSITION METAL CATALYSIS

Yaqun Zhu, M.S.

University of Pittsburgh, 2015

Catalysts accelerate rates of chemical reactions, and there is great interest in identifying catalysts that are effective, stable, and economical. This thesis reports two homogeneous chemical reaction mechanism studies using first principles quantum chemistry. The goal of this work is to understand the fundamental reaction pathways that reactions occur, so that one might eventually make improved catalysts. A cobalt-based catalyst system was recently reported for CO_2 hydrogenation to form formate.[1] It was hypothesized that a cooperative bifunctional catalyst involving an *N*-heterocyclic carbene (NHC) and this cobalt-based catalyst might further improve this chemistry. We investigated the likelihood that the NHC could function either as a Brønsted base to deprotonate a metal hydride or dihydrogen intermediate, or as a Lewis base to activate carbon dioxide towards nucleophilic attack. We also investigated fundamental catalysis involving heterobimetallic catalysts. We elucidated a complete mechanistic pathway for C−H boralytion with Cu−Fe catalysts to explain experimental observations and suggest improvements to the catalyst. This thesis aims to provide useful insight into canonical organometallic reaction mechanisms involved in bimetallic catalysts.

TABLE OF CONTENTS

LIST OF TABLES

LIST OF FIGURES

PREFACE

I wish to thank Professor John Keith for his generous support and detailed scientific guidance. He leads me patiently and systematically to think as an academic researcher. I hope that I will carry on the values and commitment to success that I have learned from him. I would like to thank my present and former Keith group members, Aude, Mitchell, Nguven, Karthikeyan, and Victor for their selfless help and valuable discussions. We had a good time together, which I will cherish forever. I would also like to thank the SAM team, especially Albert, for the continued support in my computational endeavors. Meanwhile, I would like to thank my committee members, Dr. Veser and Dr. Guofeng Wang, for their oversight. Additionally, I would like to thank the faculty, staff and students in the Chemical Engineering Department at University of Pittsburgh for their friendly treat and help.

And, my deepest gratitude goes to Junyu, and my parents. Their support and accompany make me fearless to overcome all kinds of difficulties. I greatly appreciate their endless patience. Love you.

In the end, it's not the years in our life that count. It's the life in our years. There is no formula for success, except perhaps an unconditional acceptance of life and what it brings.

1.0 INTRODUCTION

Transition metals reside in the middle of the periodic table and are defined by IUPAC as elements having incompletely filled d orbitals, which make transition metals give and take electrons easily to form one or more stable ions. These d-electrons can make transition metals play special roles in fascinating chemistry. First, they can coordinate or bind adsorbates into positions suitable for energetically efficient chemical transformations. Transition metals can also exhibit a wide range of oxidation states making them suitable for driving redox chemistry. Many transition metals exhibit versatile bonding, and this allows metals to act as homogeneous and heterogeneous catalysts, as iron does in the heterogeneous Haber Process (ammonia synthesis from nitrogen and hydrogen), nickel in the hydrogenation of C=C bonds, and vanadium(V) oxide (V_2O_5) in the contact process for producing sulfuric acid.

In heterogeneous catalysis, surface atoms at the phase boundary are catalytically active. Heterogeneous catalysis brings several practical advantages, including high densities of active sites as well as high stability that permit high reaction temperatures that can be required for overcoming thermal barriers. Alternatively, homogeneous transition metal catalysts have fewer sites and are usually less stable, but they can more easily be tailor-made with chemical modifications that permit reactions to occur at low temperatures. However, the most useful homogeneous catalysts to date have primarily been so-called "late transition metals" like Co, Fe, Rh, Ru, Ni, and Pt, since these metals exist in a coordinatively unsaturated state towards the end

1

of the transition series. Compared to the first-row transition metals, second- and third-row transition metals normally have superior activities and stabilities, but they are also not abundant (Figure 1) and much more expensive than first-row metals.
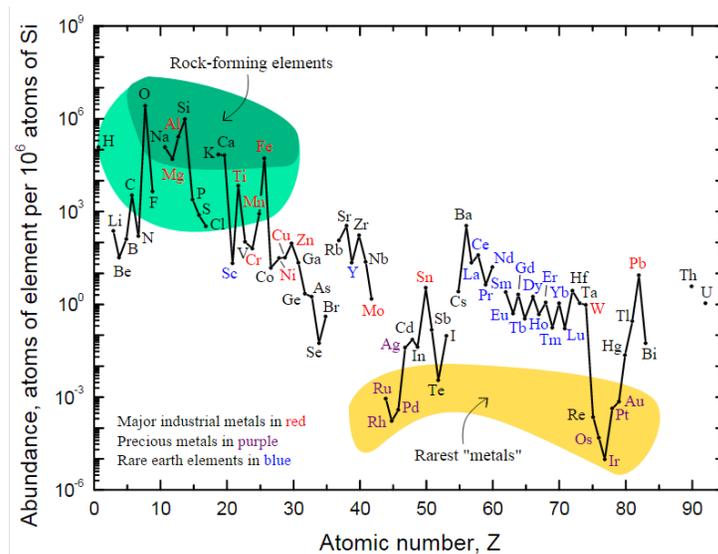
Figure 1. Relative abundance of chemical elements in Earth's upper continental crust. Numbers show percentage per million in mass. Figure taken from Ref. 2.

In order to better understand catalytic reaction mechanisms, we use first principles quantum chemistry to calculate reaction free energies. Quantum chemistry, particularly density functional theory (DFT) coupled with implicit solvation models, is used ubiquitously to study homogeneous and heterogeneous reaction mechanisms. Chapter 2 addresses a background overview of theories used as well as modern, higher level *ab initio* approaches that have potential to replace DFT for modeling homogeneous catalysis *in silico*.

There exist several homogeneous transition metal catalysts for effective CO_2 hydrogenation, but most involve non-abundant and expensive noble metals.[3,4] Non-noble metal counterparts typically have weaker hydride donating abilities, making them less prone to react with carbon dioxide. Additionally, poorly acidic metal dihydrides would limit the regeneration of

active metal hydride species.[5,6] Recently, Linehan and co-workers reported a homogeneous cobalt catalyst designed for CO_2 hydrogenation.[1] Cobalt is a relatively abundant element in nature (10-30 ppm). Intriguingly, the catalytic activity of this cobalt-based complex is comparable to the best precious metal catalysts for the production of formate from CO_2 and H_2. With the careful selection of a base whose pK_a is matched to deprotonate a cobalt dihydride complex,[1] the cobalt-based catalyst system better promotes CO_2 reduction rates than rhodium based catalysts, and with rates similar to the fastest catalysts based on iridium[4] and ruthenium[7] at room temperature. Chapter 3 addresses computational mechanistic investigations of this mechanism, as well as consideration of a hypothesized means to further improve reactivity.

Another means to improve the performance of first-row transition metals is through metal-metal cooperativity.[8] It was recently reported that C-H borylation, which normally requires Ir-based catalysts, can be activated with Cu-Fe bimetallic catalyst.[9] The cooperativity between an electrophilic Cu site and a nucleophilic Fe site enables the heterobimetallic catalyst to properties of a single-site Ir system. It indicates that new catalytic reactions could be discovered with base metal-metal cooperativity as a substitute for single–site noble metal catalysts. Chapter 4.

2.0   THEORETICAL BACKGROUND

We now provide a brief overview of fundamentals of Kohn-Sham density functional theory (DFT), continuum (also known as implicit) solvation models and a promising higher level *ab initio* theory tool, linear scaling CCSD(T), DLPNO-CCSD(T).

2.1   DENSITY FUNCTIONAL THEORY

2.1.1   Kohn-Sham DFT

According to Hohenberg-Kohn (H-K) theorems[10], the ground state properties of a many-electron system can be uniquely determined by an electron density that depends on only three spatial coordinates. Specifically, the ground state energy of a many-electron system corresponds to the minimum energy state obtained from a functional of the electron density (i.e. a density functional). However, the H-K theorems alone bring limited practical use because the universal functional form of the density functional that provides this energy is not known exactly. Today, most practical applications of DFT are carried out within the framework of Kohn-Sham (KS)[11] DFT, where the challenging problem of addressing energies of interacting electrons within the density is treated with a static external potential that is mapped onto a non-interacting system of electrons moving in a common effective potential using fictitious orbitals generated from the

density. The overall ground-state density of the this system is identical to the real system and then simply becomes the sum of densities of the occupied (occ) orbitals

$$\rho(r) = \sum_{n,occ} |\psi_n(r)|^2 \tag{1}$$

The energy functional in KS-DFT is

$$E[\rho] = T_s[\rho] + \int V_{ext}(r)\rho(r)dr + J[\rho] + E_{xc}[\rho] \tag{2}$$

The first term, T_s, is the non-interacting electron kinetic energy. The kinetic energy for a non-interacting system of electrons is the sum of the individual electronic kinetic energies. The second term is the electrostatic interaction of the electron density with an external potential V_{ext}, such as the electron-ion potential. J is the classical Hartree repulsion energy, and E_{xc} is the exchange-correlation energy for all non-classical electron-electron interactions, together with the difference in kinetic energy between the non-interacting system and the real system.

The KS wavefunction is a single Slater determinant constructed from a set of one-electron orbitals representing the spatial distribution of these non-interacting electrons, which are the lowest energy solutions to KS-DFT equations. The KS orbitals and their energies are obtained as the eigenfunctions and eigenvalues in the self-consistent solution of the KS equations

$$(-\frac{\nabla^2}{2} + V_{ext}(r) + V_H([\rho];r) + V_{xc}([\rho];r)\psi_n(r) = \epsilon_n\psi_n(r) \tag{3}$$

where, V_{ext} is the external potential, V_H is the Hartree potential, V_{xc} is the exchange-correlation potential, ψ_n is the KS wavefunction, and ϵ_n is the KS orbital energy.

2.1.2 Exchange correlation functionals, and hybrid DFT

The KS formulation in principle is exact, and would reproduce the physical electron density if the actual form of the exchange-correlation potential, V_{xc}, is known exactly. However, the actual

form of V_{xc} is not known, and so one must introduce approximate functionals based on the electron density. The search for an accurate exchange-correlation functional is one of the greatest challenges in DFT.[12]

The oldest and simplest approximation is the local density approximation (LDA), where V_{xc} for an electron is equal to that of an electron in a uniform gas of interacting electrons. The exact exchange correlation energy for a homogeneous electron gas was calculated by Ceperley and Alder using quantum Monte Carlo simulations,[13] and there are a number of functional forms using this data.[14,15] Actually, although LDA works quite well for materials with nearly homogeneous electron densities, inaccuracies result when modeling large density fluctuations within the system (i.e. molecules). More sophisticated functionals have been developed, as shown in the "Jacob's ladder" of functionals (Figure 2). The next level up is the generalized gradient approximation (GGA)[16], which improves upon the LDA formulation by expressing the exchange correlation energy as a functional of both the local density and the gradient of the density, therefore providing a better description of systems with inhomogeneity in the electron density. BLYP is obtained by adding gradient corrections to LDA formulation, specifically the Becke exchange functional[17] (B) and the correlation functional of Lee, Yang and Parr[18] (LYP). BP86 uses the same Becke 88 exchange functional as in BLYP together with the older Perdew 86 (P) correlation functional.[19]
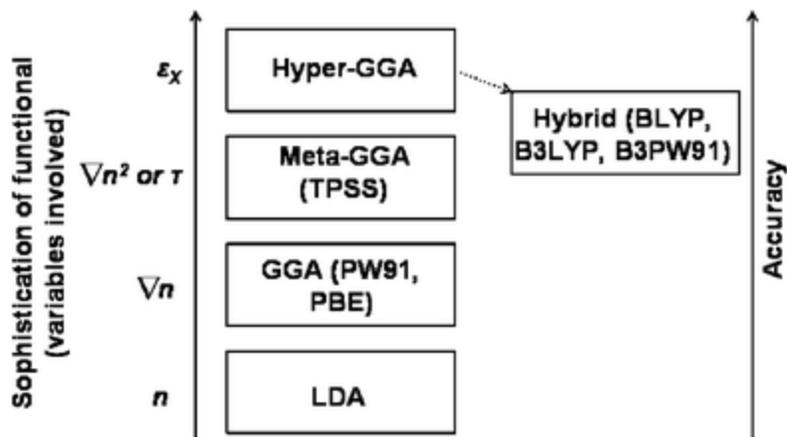
Figure 2. Schematic of relationship between commonly used exchange correlation functionals, increasing sophistication of treatment of exchange and correlation, and accuracy. Reproduced from Ref. **20** with permission of The Royal Society of Chemistry.

Using approximate exchange correlation functionals results in inexact cancellation of self-interaction energies between electrons that arise from the mean field of the Hartree energy. The self-interaction error results in excess electron delocalization, which is especially significant in systems with highly localized electrons such as the *d*-electrons in late first row transition metals and their oxides. This interaction would be cancelled exactly by the exact exchange component in HF theory. The basic idea behind the hybrid functional is to correct errors in GGA functionals by mixing in exchange energies calculated in an exact manner by using the Hartree-Fock (HF) method. Hybrid approximations for exchange-correlation functionals thus include a certain amount of the exact Hartree-Fock exchange energy mixed in with DFT approximate exchange. Hybrid functionals can offer a better description of electron-electron interactions by introducing a nonlocal exact exchange potential. DFT exchange tends to underestimate ionicity and the band gap, so adding in HF exchange, which in practice overestimates those same

7

quantities, is a reasonable means of creating favorable error cancellation. The popular B3LYP exchange-correlation functional[21] is

$$E_{xc}^{B3LYP} = E_x^{LDA} + 0.20\,(E_x^{HF} - E_x^{LDA}) + 0.72\,(E_x^{GGA} - E_x^{LDA}) + E_c^{LDA} + 0.81\,(E_c^{GGA} - E_c^{LDA}) \quad (4)$$

where, E_x^{GGA} and E_c^{GGA} are the Becke 88 exchange functional and the LYP correlation functional, E_c^{LDA} is the local-density approximation to the correlation functional.

2.2   LINEAR SCALING CCSD METHODS

2.2.1   Coupled cluster method

Inexact DFT exchange correlation functionals are a practical way to calculate electronic energies. However, exact methods that are as practical to carry out would be preferred. Coupled cluster (CC) methods[22] are one of the most robust and prevalent approaches in quantum chemistry for the computation of atomic and molecular electronic structures. In contrast to HF or DFT methods, CC methods reliably calculate the electronic correlation energies of systems that can be described with a single electronic configuration with the non-relativistic Schrödinger equation to better than chemical accuracy (defined as 1 kcal/mol in relative energies).[23] CCSD(T) (coupled cluster singles doubles perturbative triples) method is often referred to as the 'gold standard' of quantum chemistry, due to its excellent accuracy in computing reliable energies of molecules that are well described by a single reference wavefunction. CC calculations take the basic HF method and introduce electron correlation through exponential cluster operators to construct multi-electron wavefunctions. This enables correct scaling of correlation energy with respect to the number of electrons (i.e. size consistency), a problem that

plagues other ab initio methods such as CISD.[24] Since CC calculations are much more sensitive to basis sets than DFT calculations, they require large basis sets or extrapolation techniques to obtain high accuracy. However, the high accuracy also brings very poor scaling of calculation cost with respect to system size. Thus, the application of CC calculations is normally limited to systems of 10 or 20 atoms. Thus, there is a need for developing approximations to CC method that retain its accuracy but reduce the computational expense so that CC methods can be more widely used in application to large molecules.

2.2.2 LPNO-CCSD and DLPNO-CCSD(T)

The severe scaling problem of CC methods cost has led to the development of local correlation methods, such as local pair-natural orbital (LPNO)[25]-CC and domain based LPNO (DLPNO)[26]-CC methods, which allow CC calculations to be performed on larger systems than ever before. LPNO-based correlation methods are efficient and accurate and hold an enormous potential for chemical applications in both closed-shell and open-shell systems. LPNO-CCSD is an efficient local coupled cluster method with single and double excitations based on the concept of pair natural orbitals (PNOs). This method performed excellently for molecules with up to about 50-70 atoms, and the electronic correlation calculation takes 2-4 times the time required for the preceding HF calculation. Additionally, it is nearly linear scaling with respect to system size. As shown in Figure 3, the LPNO-CCSD method performs as well as pure CCSD (deviations do not exceed 0.05 kcal/mol) whereas B3LYP rotational curves show greater deviations, especially in predicting relative torsional barriers.
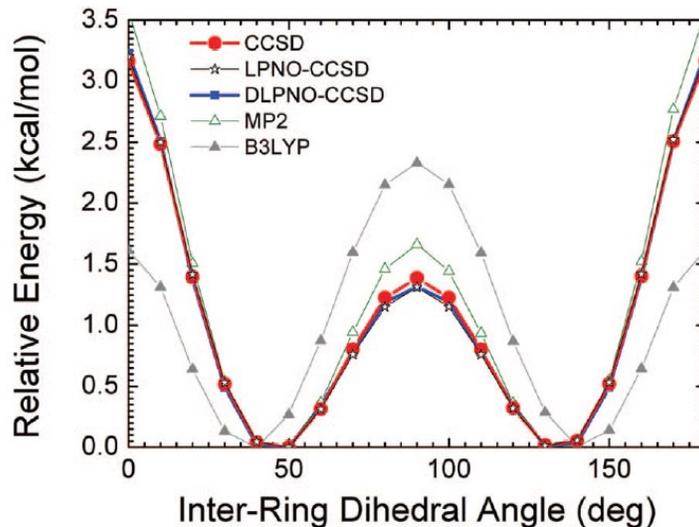
Figure 3. Rotational barrier of biphenyl. The structures from a relaxed surface scan with the PBE functional and TZVP basis set together with van der Waals corrections. All calculations were done with the SV(P) basis set. Figure taken from Ref. **25.** Reprinted with permission from [Riplinger, C.; Neese, F. An Efficient and Near Linear Scaling Pair Natural Orbital Based Local Coupled Cluster Method. *J. Chem. Phys*. 138, 034106 (2013)]. Copyright [2013], AIP Publishing LLC.

DLPNO-CCSD(T) is constructed by DLPNO correlation approaches extended to perturbative triple excitations. This approach is also nearly linear scaling with system size and can be performed for very large calculations, but for now this method is only applied for closed shell energies. Using the DLPNO-CCSD(T) approach it was possible for the first time to perform a CCSD(T) level calculation on an entire protein with more than 650 atoms. In Figure 4, DLPNO-CCSD(T) method shows a perfectly smooth behavior and follows the CCSD(T) curve nearly perfectly within a deviation range of 0.4 kcal/mol. It is obvious in **Error! Reference source not found.** that DLPNO-CCSD(T) is always much faster than canonical CCSD(T) method and DLPNO-CCSD(T) method scales approximately linearly.
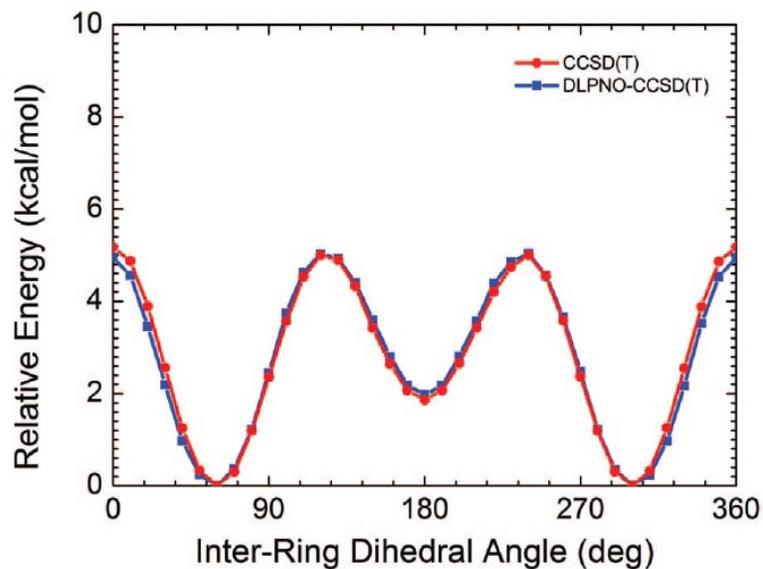
(a)
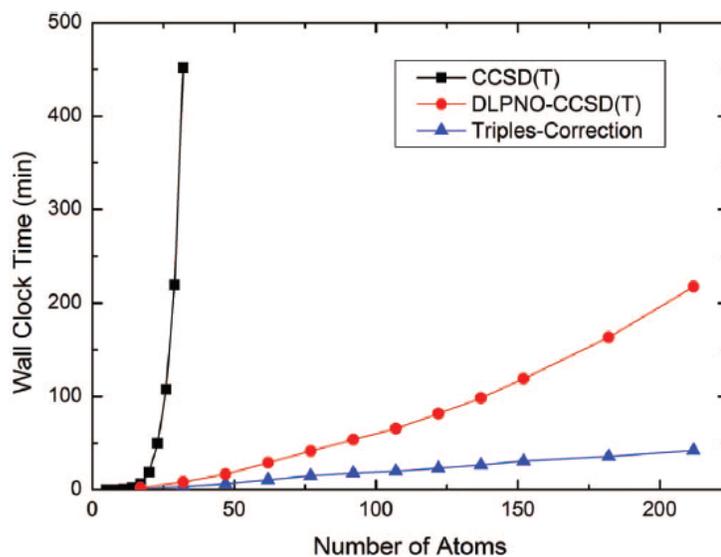
(b)

Figure 4. (a) Rotational barrier of ethane-1.2-diphenyl. The structures from a relaxed surface scan with the PBE functional and TZVP basis set with van der Waals corrections. All calculations were done with TZVP basis set. (b) Scaling behavior of the CCSD(T) and DLPNO-CCSD(T) method. The calculations were carried out on linear hydrocarbon chains H_3C-$(CH_2)_{n-2}$-CH_3. All calculations were done with the SVP basis set. The time required for triples-correction is part of the entire DLPNO-CCSD(T) calculation time. Figure taken from Ref. **26**. Reprinted with permission from [Riplinger, C.; Sandhoefer, B.; Hansen, A.; Neese, F. Natural Triple Excitations in Local Coupled Cluster Calculations with Pair Natural Orbitals. *J. Chem. Phys.* 139, 134101 (2013)]. Copyright [2013], AIP Publishing LLC.

2.3   CONTINUUM SOLVATION

Continuum solvation models extract a solvation energy by treating solvents as a continuous medium instead of individual explicit solvent molecules. By omitting solvent molecules from the calculation, continuum solvation approaches are drastically less computationally expensive. The main parameter in continuum solvation model is dielectric constant, ε, used to define the degree of polarizability of the solvent. Most implicit solvation calculations construct and then iteratively solve an effective Hamiltonian whereby the electrostatic problem is solved by considering a dielectric interacting with a cavity surface that surrounds the electron density of the molecule. The actual solvation energy value from a solvation calculation is the energy difference between two separate calculations run by the solvation module using the same level of theory and basis set. The module first computes a single-point self-consistent field (SCF) gas-phase reference energy and then the energy of the effective Hamiltonian using the electronic densities of the solvated orbitals.

2.3.1   Solvation model based on density (SMD)[27]

The SMD model is a universal continuum solvation model where "universal" denotes its applicability to any charged or uncharged solute in any solvent or liquid medium for which a few key descriptors are known. The SMD model tries to determine the solvation free energy by using the full solute electron density without determining partial atomic charges. The solvent is not presented explicitly as a collection of discrete solvent molecules but rather as a dielectric medium with surface tensions at the solute-solvent interface.

SMD directly calculates the solvation free energy of an ideal solvation process that occurs at fixed concentration (for example, from an ideal gas at a concentration of 1 mol/L to an ideal solution at a liquid-phase concentration of 1 mol/L) at 298 K, but this may be converted by standard thermodynamic formulas to a standard-state free energy of solvation, which is defined as the transfer of molecules from an ideal gas at 1 bar to an ideal 1 molar solution.

The SMD model separates the fixed-concentration solvation free energy into two components. The first component is the bulk-electrostatic energy arising from a self-consistent reaction field (SCRF) treatment. The SCRF treatment involves an integration of the nonhomogeneous-dielectric Poisson equation for bulk electrostatics in a similar way as the COSMO model of Klamt and Schüürmann[28] with the modified COSMO scaling factor suggested by Stefanovich and Truong[29] and by using the SMD intrinsic atomic Coulomb radii. These radii have been optimized for H, C, N, O, F, Si, P, S, Cl, and Br. For any other atom the current implementation of the SMD model uses scaled values of the van der Waals radii of Mantina et al.[30] The scaling factor equals 1.52 for group 17 elements heavier than Br (i.e., for I and At) and 1.18 for all other elements for which there are no optimized SMD radii.

The second contribution to the fixed-concentration free energy of solvation is the cavity-dispersion-solvent-structure (CDS) term, a contribution arising from short-range interactions between the solute and solvent molecules in the first solvation shell. This contribution is a sum of terms that are proportional (with geometry-dependent proportionality constants called atomic surface tensions) to the solvent-accessible surface areas (SASAs) of the individual solute atoms.

2.3.2 Conductor-like screening model (COSMO)[28]

COSMO is another dielectric continuum solvation model used to determine the electrostatic interaction of a molecule with a solvent. It has become very popular due to its algorithmic simplicity, numerical stability, and relative insensitivity with respect to outlying charge errors. COSMO approximates the solvent by a dielectric continuum with a permittivity surrounding the solute molecules outside of a molecular cavity. Generally, the solvent model is constructed as an assembly of atom-centered spheres with radii approximately 20% larger than the Van der Waals radius. However, cavity construction differs in different COSMO implementations.

The COSMO method can be used for all methods in theoretical chemistry where the charge distribution of a molecule can be determined, for example, in semiempirical calculations, HF method calculations or DFT calculations. COSMO derives the polarization charges of the continuum caused by the polarity of the solute from a scaled-conductor approximation. Based on the solvent charges and the charge distribution of the molecules, the interaction energy between the solute molecule and the solvent can be calculated.

2.4   CALCULATION SCHEMES

2.4.1   Total Gibbs free energy

The geometry optimizations were performed using DFT with one exchange-correlation functional (B3LYP or BP86), additionally the "resolution of the identity" (RI) approximation[31], and double-zeta basis set.[32] Single-point energy calculations on the optimized geometries were

carried out with the same functional and a larger basis set, or using LPNO-CCSD. Dispersion interactions accounted for using Grimme's D3 dispersion correction scheme[33] were applied to all DFT calculations. All stationary structures were characterized by vibrational frequency analysis employing the harmonic oscillator approximation, either as stable intermediates with zero imaginary frequencies or as transition states with only one imaginary frequency. Vibrational energy contributions to energies were calculated so that any frequency lower that 50 cm⁻¹ was substituted with a value of 50 cm⁻¹ to minimize the effect of spurious errors in entropy calculations due to very small vibrational modes. An appropriate scaling factor was employed for the vibrational frequencies. The thermochemical contributions were calculated using the ideal-gas-rigid-rotor-harmonic-oscillator (IGRRHO) approximations at a temperature of 298.15 K.

Solvation effects were treated using implicit solvation models, SMD or COSMO. Calculated values were corrected by 1.89 kcal/mol for the change in standard states from gas phase (1 atm) to condensed phase (1 M).[34] The total Gibbs free energy (G) for all species at T = 298 K was computed as

$$G^o_{298} = E_{SCF} + ZPE + H_{298} - TS_{298} + \Delta G_S + 1.89 \; kcal/mol \qquad (5)$$

where, E_{SCF} is the electronic energy from the quantum chemistry calculations, ZPE is the zero-point energy from the harmonic oscillator approximation, H_{298} and S_{298} are the total thermal and entropic energies from IGRRHO approximations, and ΔG_S is the solvation energy.

2.4.2 Proton and hydride energies

Aqueous phase deprotonation free energies of a Brønsted acid were derived by using the thermodynamically consistent cycle[34]
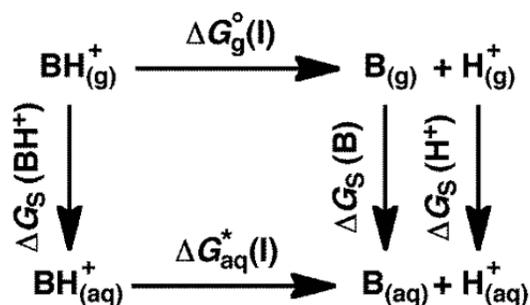
Finally, the deprotonation free energy was calculated using

$$\Delta G^*_{aq}(l) = \Delta G^o_g(l) + \Delta G_s\ (B) + \Delta G_s\ (H^+) - \Delta G_s\ (BH^+) \tag{6}$$

and pK_a was linked to the free energy using[35]

$$pK_a = \frac{\Delta G^*_{aq}(l)}{2.303\ RT} \tag{7}$$

The free energy of a gaseous proton, $G(H^+_{(g)})$, was calculated as -6.3 kcal/mol from the Sackur$-$Tetrode equation.[36] The smallest feasible model for a proton in solution would be hydronium, H_3O^+, since H^+ does not involve any electron. However, Zundel ($H_5O_2^+$) or Eigen ($H_9O_4^+$) might be more physical models for a proton in solution. There are numerous empirical values in the literature for proton solvation energy, $\Delta G_s(H^+)$.[37,38] Currently, the most accurate value of $\Delta G_s(H^+)$ was provided by the cluster ion experiments by Tissandier et al.[39] $\Delta G_s(H^+)$ was taken as -264.0 kcal/mol, which already includes the free energy contribution needed for the aqueous proton to have a standard state of 1 M.

For hydricity calculations, the absolute energy of an aqueous phase hydride, H^-, was calculated using the gas phase energy of H_2 to plus the energy for H_2 heterolysis in solution, $\Delta G_{hetero}(H_2)$, and then to minus the absolute energy of an aqueous phase proton.

3.0 CO_2 HYDROGENATION CATALYSTS AND CATALYSIS

3.1   INTRODUCTION TO CO_2 REDUCTION

Recently, climate change and its impact on the earth and society has been reassessed by the International Panel on Climate Change. The panel estimates that the greenhouse gas emissions should be reduced by half by 2030 to mitigate climate change. CO_2 conversion is strongly desired to help with this goal, since CO_2 is a greenhouse gas, released by natural and artificial processes. The reduction of CO_2 to useful chemicals using carbon-neutral energy is also an alternative to the depletion of fossil resources.[40]

Due to the remarkable thermodynamic stability of CO_2, the chemical reduction of CO_2 is energetically uphill. CO_2 conversion process requires a significant amount of energy. Achievements in the fields of photocatalysis during the last decade sparked increased interest in the possibility of using sunlight to reduce CO_2. Solar energy can be stored in chemical bonds through the conversion of CO_2 to fuels. With the aid of enzymes, nature uses this strategy to address its own energy needs. Natural enzymes can utilize exogenous base residues to convert stable small molecules like CO_2 to useful fuels.[41] Over the past decade, photo-electrochemical water splitting has made significant progress, making it economically feasible to produce H_2 from a renewable resource.[42] One possible chemical approach for CO_2 conversion would be to

generate H_2 firstly via photo-electrochemical processes using electrical power from photovoltaic cells or wind turbines, and then use H_2 for hydrogenation of CO_2, as in eq 8.

$$H_2 + CO_2 + base \leftrightarrow HCO_2^- + base - H^+ \tag{8}$$

However, the chemical route of CO_2 conversion requires the development of catalysts based on abundant metals.

3.2 CO_2 HYDROGENATION WITH A COBALT-BASED CATALYST

3.2.1   Catalytic cycle for CO_2 hydrogenation with $Co(dmpe)_2H$

Recently, molecular catalysts research has improved rates of CO_2 conversion to formate. However, most of the best catalysts are based on precious metals like rhodium, iridium, and ruthenium,[43,44] which are scarce and expensive. Compared to noble metal catalysts, non-noble metal catalysts have weaker hydride donor abilities making hydrides less prone to reactions with carbon dioxide. However, improving the hydricity sometimes limit catalytic turnover due to slow conversion into active metal hydride species.[5,6]

Linehan recently developed a catalyst system containing cobalt-hydride bis-diphosphine complex, $Co(dmpe)_2H$ (where dmpe is 1,2-bis(dimethylphosphino)-ethane), which has high catalytic activity even under ambient conditions.[1] As shown in Figure 5, this catalytic system can both transfer a hydride to CO_2 (ΔG_{H^-}) and form a dihydride cation that is sufficiently acidic (pK_a) to be deprotonated for the regeneration of $Co(dmpe)_2H$.
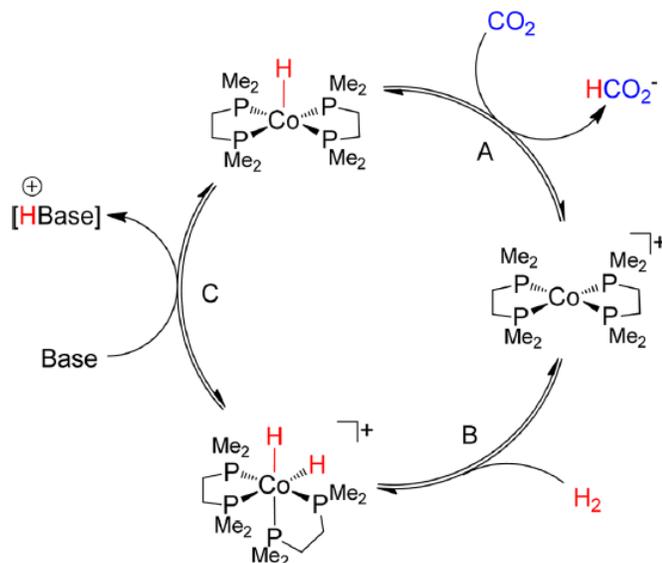
Figure 5. Proposed catalytic cycle for CO_2 hydrogenation using $Co(dmpe)_2H$. Figure taken from Ref. 1. Reprinted with permission from (Jeletic, M. S.; Mock, M. T.; Appel, A. M.; Linehan, J. C. A Cobalt-Based Catalyst for the Hydrogenation of CO_2 under Ambient Conditions. *J. Am. Chem. Soc.* 135, 11533-11536 (2013)). Copyright (2013) American Chemical Society.

M-H bond of $Co(dmpe)_2H$ is sufficiently weak to react with CO_2 to produce formate, step A in Figure 5. This hydride transfer reaction has a free energy of -8 kcal/mol, which is defined by the difference in the heterolytic bond strengths of $Co(dmpe)_2H$[6,45] and formate[43,44], eq 9 and 10.

$$Co(dmpe)_2H \rightarrow Co(dmpe)_2^+ + H^- \qquad \Delta G_{H^-} = + 36 \text{ kcal/mol} \qquad (9)$$

$$CO_2 + H^- \rightarrow HCO_2^- \qquad - \Delta G_{H^-} = - 44 \text{ kcal/mol} \qquad (10)$$

$$Co(dmpe)_2H + CO_2 \rightarrow Co(dmpe)_2^+ + HCO_2^- \qquad \Delta G_{H^-} = - 8 \text{ kcal/mol} \qquad (11)$$
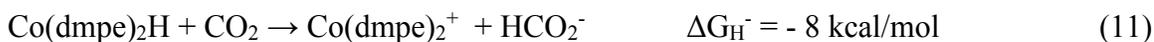
The regeneration process of $Co(dmpe)_2H$ is the oxidative addition of H_2 to the $Co(dmpe)_2^+$, step B in Figure 5, with the following deprotonation of the resulting cobalt-dihydride, $Co(dmpe)_2H_2^+$. The cobalt dihydride intermediate has a pK_a value of 33.7 in

acetonitrile phase[5], and requires a base that has a conjugate acid with a similar or higher pK_a value.

3.2.2 Computational methods calibration

The hydride transfer reaction free energies appeared in Linehan's recent work were computed using our thermodynamically consistency cycle. Geometry optimization and vibrational frequency calculations were carried out for all the intermediates using TURBOMOLE[46] with B3LYP or BP86 exchange correlation functional, employing RI approximation. The def2-SVP basis set was used along with the corresponding def2-SVP/J auxiliary basis set.[32,47] The coordinates optimized from TURBOMOLE were then used with def2-TZVP basis set for single-point electronic energy calculations. In all DFT calculations, the Grimme D3 dispersion correction was applied. Single-point energies were also computed using LPNO-CCSD and DLPNO-CCSD(T) with the minimally augmented def2-SVP and def2-TZVP basis sets[47,48] for all atoms in the ORCA program package.[49] Two-point extrapolation scheme with extrapolation parameters $\alpha = 3.4$ and $\beta = 2.4$ were used to get the activation barriers at the complete basis set.[50] The zeroth-order regular approximation (ZORA) was employed for scalar relativistic effects.[51,52] Solvation energies (ΔG_s) for all intermediates in acetonitrile phase were calculated using def2-TZVP basis set and two different solvation models, SMD in GAMESS-US and COSMO in TURBOMOLE. The $\Delta G_s(H^+)$ value for a proton in acetonitrile was taken as -260.2 kcal/mol, which does not include the $+1.89$ kcal/mol free energy contribution needed to achieve an solvent phase standard state of 1 M. The energy for H_2 heterolysis in acetonitrile, $\Delta G_{hetero}(H_2)$, was taken as $+76.0$ kcal/mol[44].

Table 1 lists the reported and our computational reaction energies for eq. 9 to 11 in terms of different calculation methods. The superscripts describe the level of theory. For example, ΔG_g^{BP86} is the relative gas phase Gibbs free energy for intermediates whose geometry optimization and single point energy calculations were performed using the BP86 functional. $\Delta G_g^{B3LYP,LPNO-CCSD}$ indicates geometry optimization of the intermediates carried out with B3LYP functional in TURBOMOLE together with single-point energies from LPNO-CCSD calculations in ORCA.

Table 1. Reaction free energies (kcal/mol) for the reaction in Linehan's work.

Reaction	2	3	4
Reference	36[6,45]	-44[43,44]	-8
$\Delta G_g^{B3LYP} + \Delta G_s^{B3LYP,COSMO}$	38.6	-55.0	-16.4
$\Delta G_g^{B3LYP,LPNO-CCSD} + \Delta G_s^{B3LYP,COSMO}$	51.1	-58.7	-7.6
$\Delta G_g^{B3LYP,DLPNO-CCSD(T)} + \Delta G_s^{B3LYP,COSMO}$	59.3	-59.1	0.2
$\Delta G_g^{B3LYP} + \Delta G_s^{B3LYP,SMD}$	35.8	-44.3	-8.5
$\Delta G_g^{B3LYP,LPNO-CCSD} + \Delta G_s^{B3LYP,SMD}$	48.3	-48.0	0.3
$\Delta G_g^{B3LYP,DLPNO-CCSD(T)} + \Delta G_s^{B3LYP,SMD}$	56.5	-48.4	8.1
$\Delta G_g^{BP86} + \Delta G_s^{BP86,COSMO}$	47.1	-53.7	-6.6
$\Delta G_g^{BP86,LPNO-CCSD} + \Delta G_s^{BP86,COSMO}$	50.1	-56.7	-6.6
$\Delta G_g^{BP86,DLPNO-CCSD(T)} + \Delta G_s^{BP86,COSMO}$	58.3	-57.0	1.3
$\Delta G_g^{BP86} + \Delta G_s^{BP86,SMD}$	44.1	-43.1	1.0
$\Delta G_g^{BP86,LPNO-CCSD} + \Delta G_s^{BP86,SMD}$	47.2	-46.1	1.1
$\Delta G_g^{BP86,DLPNO-CCSD(T)} + \Delta G_s^{BP86,SMD}$	55.4	-46.4	9.0

Of all the calculation methods, $\Delta G_g^{B3LYP} + \Delta G_s^{B3LYP,SMD}$ calculation results are in best overall agreement with the reported data. The predicted hydride transfer reaction energies

calculated with this method were within 0.5 kcal/mol of the experimental value. We also

calculated pK_a value of the dihydride intermediate, $Co(dmpe)_2H_2^+$. $\Delta G_g^{B3LYP} + \Delta G_s^{B3LYP,SMD}$

gives the same pK_a value, 33.7,[44] as reported.

Table 2. pK_a value of cobalt dihydride complex.

Method	pK_a
Reference	33.7[44]
$\Delta G_g^{B3LYP} + \Delta G_s^{B3LYP,COSMO}$	30.9
$\Delta G_g^{B3LYP,LPNO-CCSD} + \Delta G_s^{B3LYP,COSMO}$	28.4
$\Delta G_g^{B3LYP,DLPNO-CCSD(T)} + \Delta G_s^{B3LYP,COSMO}$	22.8
$\Delta G_g^{B3LYP} + \Delta G_s^{B3LYP,SMD}$	33.7
$\Delta G_g^{B3LYP,LPNO-CCSD} + \Delta G_s^{B3LYP,SMD}$	31.2
$\Delta G_g^{B3LYP,DLPNO-CCSD(T)} + \Delta G_s^{B3LYP,SMD}$	25.6
$\Delta G_g^{BP86} + \Delta G_s^{BP86,COSMO}$	26.7
$\Delta G_g^{BP86,LPNO-CCSD} + \Delta G_s^{BP86,COSMO}$	27.9
$\Delta G_g^{BP86,DLPNO-CCSD(T)} + \Delta G_s^{BP86,COSMO}$	21.6
$\Delta G_g^{BP86} + \Delta G_s^{BP86,SMD}$	29.6
$\Delta G_g^{BP86,LPNO-CCSD} + \Delta G_s^{BP86,SMD}$	30.8
$\Delta G_g^{BP86,DLPNO-CCSD(T)} + \Delta G_s^{BP86,SMD}$	24.5

Given that our results for the two solvation models are relatively uncertain by ~3-10 kcal/mol, we also considered small molecules (CO_2, and HCO_2^-) treated with an extra explicit solvent molecule in a cluster-continuum approach.[53] The energies obtained with this method, however, (e.g. eq. 11) deviated more with respect to the experimental value. In principle, more acetonitrile molecules should be considered for a more accurate solvation energy. Considering the computational cost and the necessity of these data for the reaction energy calculation, we have not run calculations to determine the solvation energies of these small molecules.

3.3 CO₂ HYDROGENATION WITH BIFUNCTIIONAL CATALYSTS

3.3.1 Background and significance

Our collaborator, Prof. Jeffery Byers of Boston College, hypothesized that cooperative catalysts involving a base catalyst and a transition metal catalyst would result in unique reactivity for the activation and functionalization of small molecules. To assess the validity of this hypothesis, we modeled a cooperative bifunctional catalyst that incorporates a non-noble metal catalyst, $Co(dmpe)_2H$, and an organic base, *N*-heterocyclic carbine (NHC) for the hydrogenation reaction of carbon dioxide to formic acid.

In principle, improved reaction rates might be achieved by one of two cooperative reaction mechanisms: (1) the NHC will act as a catalytic Brønsted base to deprotonate a metal hydride or dihydrogen intermediate in Figure 6a, (2) the NHC will act as a Lewis base to activate carbon dioxide towards nucleophilic attack in Figure 6b. The benefits of incorporating a Brønsted base and $Co(dmpe)_2H$ for cooperative catalysis in CO_2 hydrogentaion was highlighted in Linehan's work, and a base is required to achieve high catalytic turnover. Since that imidazolium salts ($pK_a \sim 25$) can be deprotonated to be catalytic by organic bases whose conjugate acids have a much lower pK_a,[54,55] a bifunctional catalyst based on NHC acting as a Brønsted base is feasible. On the other hand, free NHC molecules react with CO_2 to yield zwitterionic species, similar to step i in Figure 6b. The protonation of this species would lead to the electrophilic carboxylate intermediate, which can react with the less hydridic metal hydrides. Higher catalytic turnover is expected as a result of cooperativity catalysis between the NHC as a Lewis base and $Co(dmpe)_2H$.
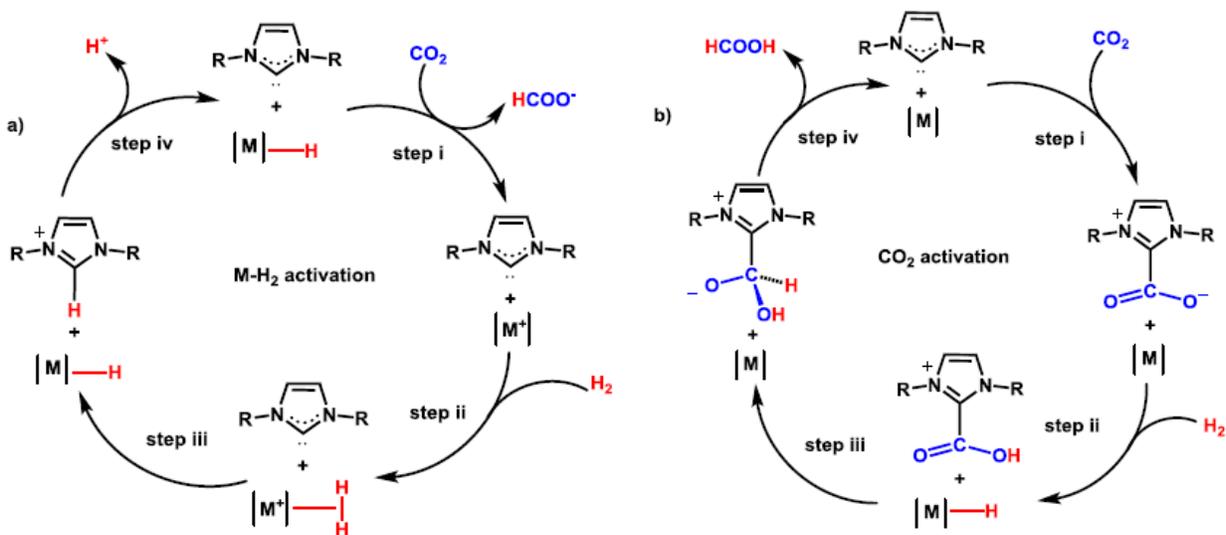
Figure 6. Mechanisms for CO_2 hydrogenation to formic acid facilitated by (a) Brønsted base or (b) Lewis base catalysis. [M^+] indicates $Co(dmpe)_2^+$. In our study, we considered R to be a methyl or phenyl group.

3.3.2 Computational methods

Based on our previous computational results in 3.2.2, reasonable agreement with experimental observation for hydride transfer was obtained using $\Delta G_g^{B3LYP} + \Delta G_s^{B3LYP,SMD}$, which was therefore used to investigate the CO_2 hydrogenation mechanisms proposed by Dr. Byers. Geometry optimizations and vibrational frequency calculations were carried out using TURBOMOLE calculations with RI-B3LYP/def2-SVP theory. Single-point electronic energy calculations were then carried out at these optimized geometries using def2-TZVP basis set. Effects from acetonitrile solvent were treated using def2-TZVP basis set and SMD solvation model with the coordinates optimized.

The full reaction mechanisms are reported in Figure 7 and Figure 9 to show relative energies of different intermediates.

25

3.3.3 Brønsted base catalysis

The catalyst system with NHC as a Brønsted base was proposed to initiate with a hydride of $Co(dmpe)_2H$ transferred to CO_2 to produce formate and the cobalt(I) complex, $Co(dmpe)_2^+$, same as in eqs 9-11. A transition state (**TS1**) was also located. The energy of **TS1** is +11.3 kcal/mol uphill relative to the energy of **1**. As shown in Figure 8, there exist attractive interactions between C and the hydride (1.71 Å). M−H bond in **TS1** is slightly lengthened from 1.50 Å to 1.56 Å.
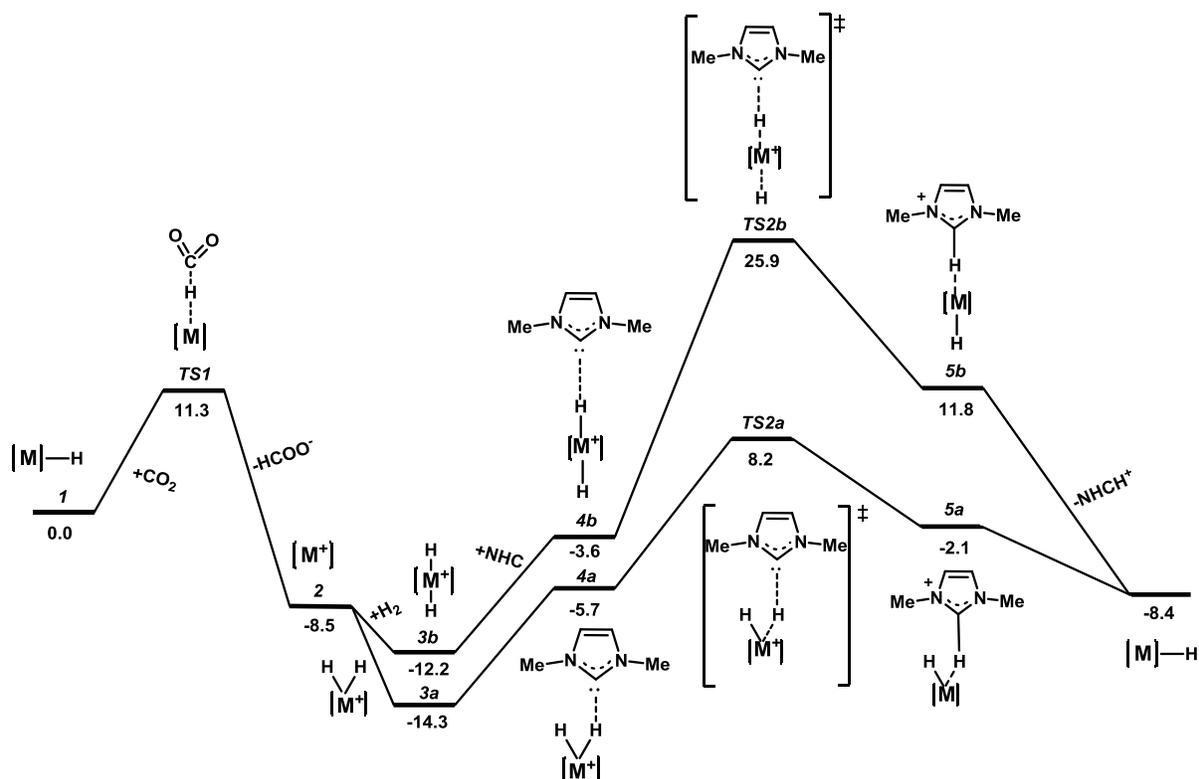
Figure 7. Full reaction mechanism for CO_2 hydrogenation to formic acid facilitated by Brønsted base catalysis. $[M^+]$ indicates $Co(dmpe)_2^+$. Relative energies referenced to **1** are shown in units of kcal/mol.

Following the oxidative addition of H_2 to the cobalt(I) complex, step ii in Figure 6a., cobalt(III)-dihydride intermediate, $Co(dmpe)_2H_2^+$, was produced. $Co(dmpe)_2H_2^+$ has two

geometric isomers, cis (complex **3a** in Figure 7) and trans (complex **3b** in Figure 7). The reaction free energies of oxidative addition of H_2 to $Co(dmpe)_2^+$ is energetically downhill. *cis*-$Co(dmpe)_2H_2^+$ is -5.8 kcal/mol downhill with respect to complex **2**, and -2.1 kcal/mol more stable than complex **3b**. Co−H bond is activated from complex **3a** and **3b** via **TS2a** and **TS2b** separately. Transition states (**TS2a** and **TS2b**, Figure 7) showed that H^+ transfers to the NHC before regeneration of $Co(dmpe)_2H$. The energy for **TS2a** is +22.5 kcal/mol, relative to complex **3a**. **TS2b** was more than 10 kcal/mol uphill relative to **TS2a** and thus the *cis*-cobalt complex was can be considered to be thermodynamically accessible. As shown in Figure 8, the metal-H bond in **TS2a** is breaking with a bond distance of 1.81Å, compared to a value of 1.48 Å in the isolated *cis*-cobalt dihydride intermediate. In complex **5a**, the C-H (1.11 Å) bond is partially formed and the Co-H (2.52 Å) bond is partially broken. The C-H bond is fully formed at a distance of 1.09 Å. The reaction between cobalt(III)-dihydride intermediate and NHC was calculated to be thermodynamically uphill by +5.9 kcal/mol for the regeneration of $Co(dmpe)_2H$.
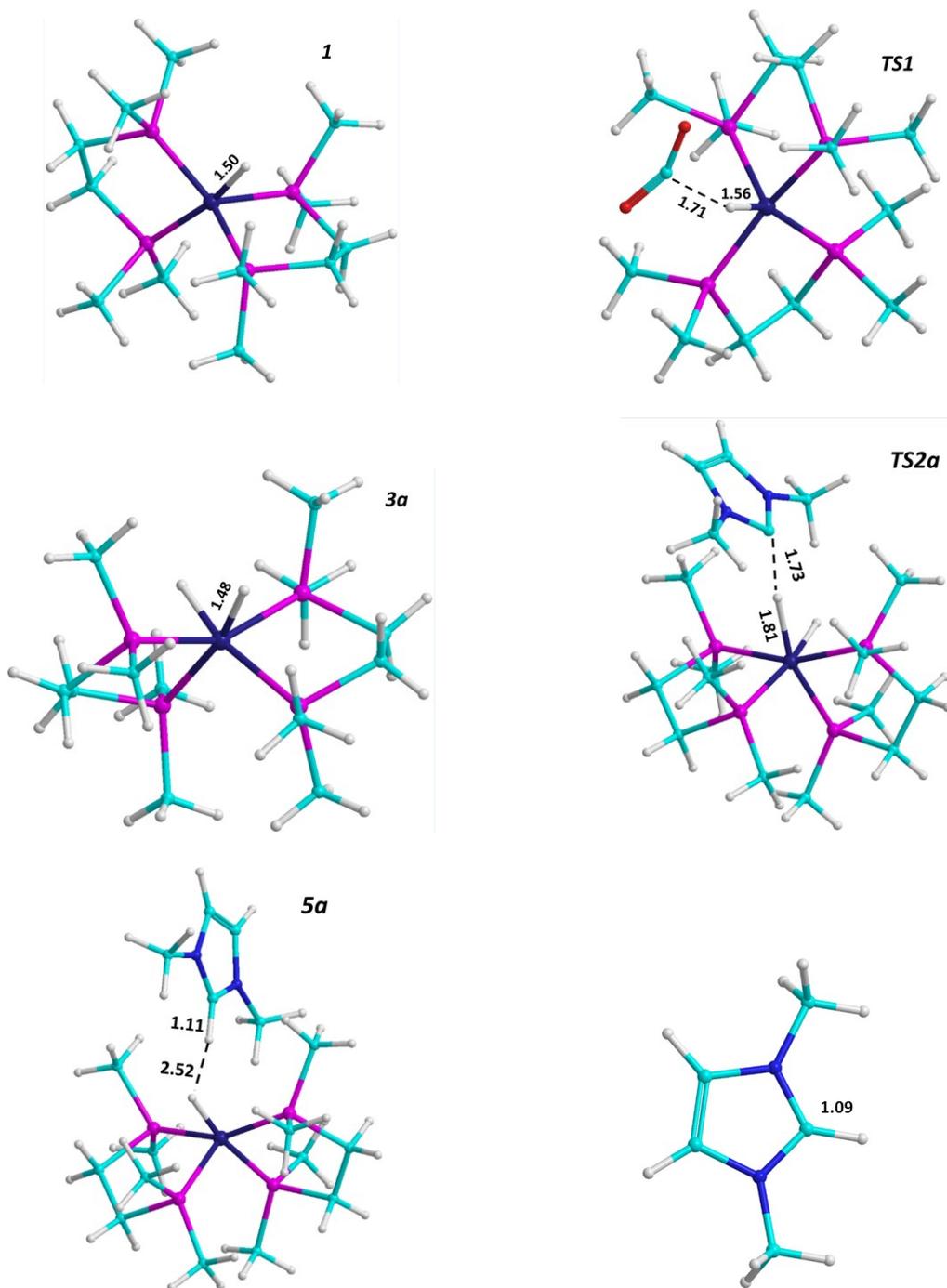
Figure 8. Reaction intermediates and transition states involved during Brønsted base catalysis. Reported interatomic distances are given in Å.

3.3.4 Lewis base catalysis

We also considered this system as a Lewis base catalyst. Here, NHC acts as a Lewis base to activate carbon dioxide towards nucleophilic attack. The reaction free energies of CO_2 reacting with carbene are downhill. As shown in Figure 9, complex **2** with the C-C bond fully formed is produced with -6.4 kcal/mol relative to **1**.

Following the combination of CO_2 to NHC, cobalt hydride intermediate and carbene formic acid were generated after H_2 dissociation. There are two possible pathways. One is the oxidative addition of H_2 to $Co(dmpe)_2^+$ to form cobalt-dihydride intermediate firstly with the following deprotonation of $Co(dmpe)_2H_2^+$ to react with carbene carboxylate (**2**→**3a/3b**→**4**). As mentioned in the Brønsted base catalysis, the reaction free energies of oxidative addition of H_2 to $Co(dmpe)_2^+$ is energetically downhill. *Cis*-$Co(dmpe)_2H_2^+$ is more stable than *trans*-$Co(dmpe)_2H_2^+$. The deprotonation of $Co(dmpe)_2H_2^+$ to produce carbene formic acid was calculated to be thermodynamically uphill by +36.3 kcal/mol for cis isomer and +34.2 kcal/mol for trans isomer. The other one is the ionic dissociation of H_2 with hydride transferred to cobalt and proton associated with carboxylate (**2**→**4**). The energy of **4** is +30.5 kcal/mol uphill relative to the energy of **2**. For both pathways, the reaction energy is over 30 kcal/mol. The activation energy barrier for this step will be > 30 kcal/mol. It is hard for this scheme to happen in reality and thus transition states were not pursued further. The reason for the high activation energy barrier may be due to that carbene carboxylate is a weak base, and will not readily accept a proton. Subsequent steps to form HCOOH and regenerate catalysts was calculated to be downhill by -17.9 kcal/mol.
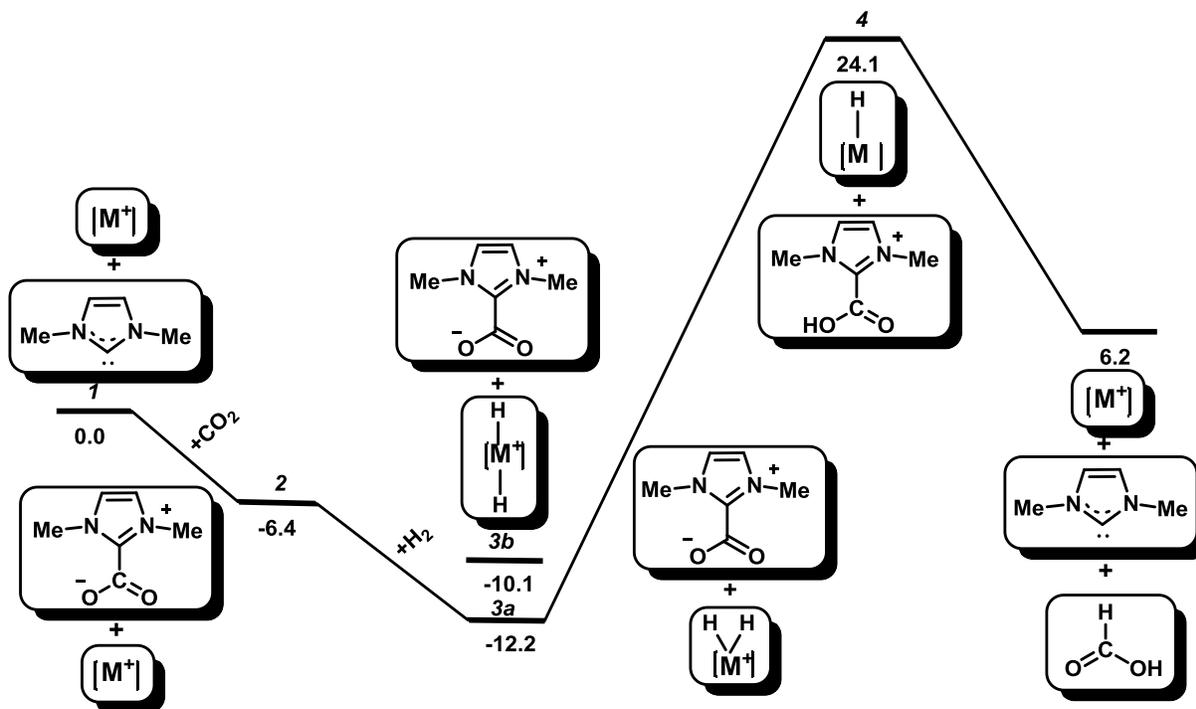
**Figure 9.** Full reaction mechanism for CO_2 hydrogenation to formic acid facilitated by Lewis base catalysis. $[M^+]$ indicates $Co(dmpe)_2^+$. Relative energies referenced to **1** are shown in units of kcal/mol.

3.3.5 Dihydride reacting with CO_2

The reaction between cobalt(III)-dihydride intermediate and CO_2 was also considered, if proton and hydride simultaneously combined to CO_2. The reaction was calculated to be thermodynamically uphill by +12.0 kcal/mol for the *cis*-$Co(dmpe)_2H_2^+$, and +9.9 kcal/mol for the *trans*-$Co(dmpe)_2H_2^+$. Attempts at locating a transition state of this process resulted in species with over 50 kcal/mol relative to reactants. Therefore, it is hard for both H^+ and H^- dissociated from cobalt(III)-dihydride intermediate to produce formic acid.

3.3.6 Ligand size effect

Because a potent Lewis base tends to bind irreversibly with transition metals, NHC with larger ligands that prevent the base from binding to the transition metal center was considered. We calculated the reaction energies of **1→2** between CO_2 and NHC with phenyl ligand in Lewis base catalysis. The relative energy with phenyl ligand is -7.7 kcal/mol instead of -6.4 kcal/mol for the methyl ligand. Since the 1.3 kcal/mol difference is within the margin of error for our DFT calculations, it cannot be interpreted as evidence that the larger ligands result in substantially lower reaction barriers.

3.3.7 Conclusions

We have characterized a full mechanistic cycle for CO_2 hydrogenation with cooperative catalysts involving NHC as a base and $Co(dmpe)_2H$ using first-principles computational quantum chemistry.

By comparing several sets of quantum chemistry calculations, we find that DFT calculations with B3LYP exchange-correlation functional in tandem with SMD solvation model gives higher accuracy for hydride transferring reaction. According to our calculation results, the catalyst system with NHC as a Brønsted base was thermodynamically feasible for the hydrogenation of CO_2 to formic acid, while high energy is required for Lewis base catalytic cycle to work.

In Brønsted base catalysis, the entire catalytic process is slightly downhill in energy by -8.4 kcal/mol. $Co(dmpe)_2H$ reacts with CO_2 to produce formate firstly with the following oxidative addition of H_2 to $Co(dmpe)_2^+$. Cobalt dihydride intermediate was deprotonated by

31

NHC for the regeneration of the catalyst for the next cycle. Since cis-Co(dmpe)$_2$H$_2^+$ is more stable than its $trans$ isomer and the activation energy for cis-cobalt complex is lower compared to $trans$-cobalt complex, the catalytic cycle with cis-cobalt complex was thermodynamically accessible.

To further improve this catalyst system, new designs should focus on better deprotonation of metal dihydride.

4.0   C-H BORYLATION BY CU-FE HETEROBIMETALLIC CATALYSTS

4.1   BACKGROUND AND SIGNIFICANCE

Organic molecules often contain multiple C-H bonds, and it is challenging to activate a specific C-H bond. The selective transformation of inert C-H bonds to other functional ligands has far-reaching practical implications. Abundant alkanes or arenes can be converted into valuable functionalized organic molecules through metal-catalyzed C-H bond activation. C-H borylation reactions are useful reactions for C-H activation by producing an organoboron compound through functionalization of alkane and arene molecules. Since the C-B bond can be converted to a C-C, C-N, C-O, or C-X(X=Br, Cl) bond, organoboron compounds can be applied for chemical synthesis. Transition metal catalyzed C-H borylation potentially provide general solutions to the regioselectivity of arene activation caused by steric effects.

C-H borylation normally requires noble metal catalysts such as those involving Ir.[56] Recently a Cu-Fe heterobimetallic C-H borylation catalyst was reported: (IPr)Cu-Fp (IPr = N,N′-bis(2,6-diisopropylphenyl)imidazol-2-ylidene, Fp = FeCp(CO)$_2$), a Cu−Fe heterobimetallic complex supported by a bulky N-heterocyclic carbene (NHC) ligand (Figure 10b).[9] Metal-metal cooperativity has been acknowledged as a source of reaction rate acceleration[57] or selectivity amplification[58] in certain scenarios, but it is rare for a homogeneous catalyst to require metal-metal cooperativity.[59] This cooperativity presumably enables the Cu-Fe paring to mimic the

33

behavior of single-site Ir systems. This would be similar to the "superatoms" in the field of cluster science, where clusters of two earth-abundant elements from disparate parts of the periodic table can mimic precious element that resides in between them on the periodic table.[8]

As shown in Figure 10, the proposed mechanism for the heterobimetallic C-H borylation reaction includes bimetallic analogues of the oxidative addition (OA) and reductive elimination (RE) reactions, which are typically accomplished by single-site noble metals, i.e., B-H bimetallic oxidative addition (BOA) and H-H bimetallic reductive elimination (BRE). To have a better understanding of how homogeneous catalysts comprised of two base metals can mimic precious metal catalysts, we provided a complete mechanistic study of C-H borylation with Cu-Fe catalysts.
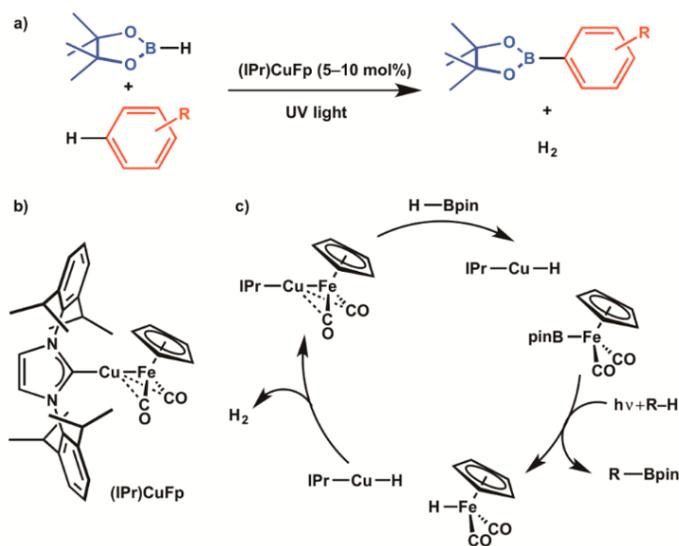
Figure 10. (a) C-H borylation catalyzed by Cu-Fe cooperativity; (b) the optimal catalyst, (IPr)CuFp; (c) proposed heterobimetallic mechanism for C-H borylation. Catalytic conditions: 450-W Hg arc lamp, ambient temperature, neat arene. Figure taken from Ref. **60**. Adapted with permission from (Parmelee, S. R.; Mazzacano, T. J.; Zhu, Y.; Mankad, N. P.; Keith, J. A. A Heterobimetallic Mechanism for C–H Borylation Elucidated from Experimental and Computational Data. *ACS Catal.* 5(6), 3689−3699 (2015)). Copyright (2015) American Chemical Society.

4.2   CALCULATED C-H BORYLATION MECHANISM

The following computational analysis of heterobimetallic C-H borylation mechanism using DFT has been published recently on ACS Catalysis.[60]

4.2.1   Computational methods

First-principles DFT calculations with B3LYP exchange correlation functional were carried out in GAMESS-US.[61] Geometry optimizations of all intermediates were performed using the LANL2DZ[62] effective core potentials (ECP) on Fe and Cu atoms (each subsuming 10 core electrons on each metal atom) and the 6-31G** basis set on all other atoms. The D3 dispersion correction of Grimme et al. was applied in all calculations. Intrinsic reaction coordinate calculations confirmed that each transition state was situated between its corresponding reactant and product states on the Born-Oppenheimer potential energy surface. Temperature–dependent energies for all species at T=298 K were computed using standard statistical thermodynamics approximations.[63] Single point electronic energy calculations were then carried out at these optimized geometries using a larger basis set where Fe and Cu atoms were treated with the LANL08(f) ECP (which utilized the same ECP as before except with fully uncontracted basis functions and an additional f function in the valence basis set), and all other atoms used the MG3S basis set[64] (a modification of the 6-311++G** basis set that includes f functions on heavy atoms). Effects from benzene solvent were treated using the SMD solvation model with default settings as implemented in GAMESS-US.

Additional calculations using larger model systems were carried out to investigate the relative importance of an additional borane molecule and the validation of the substantially

smaller (IMe)Cu (IMe = N,N′-dimethylimidazol-2-ylidene) model in place of the full (IPr)Cu moiety. Geometry optimizations and vibrational frequency calculations on these larger systems were carried out using TURBOMOLE calculations with RI-B3LYP/def2-SVP level of theory. Differences in thermal and entropic energy contributions of molecules at 298.15 K calculated with TURBOMOLE and GAMESS-US were ~0.3 kcal/mol and thus considered negligible. The coordinates optimized from TURBOMOLE were then used in GAMESS-US calculations with a larger basis set and continuum solvation for direct comparison to other data in this work.

A full reaction mechanism is reported in Figure 11 to show relative energies of different intermediates.
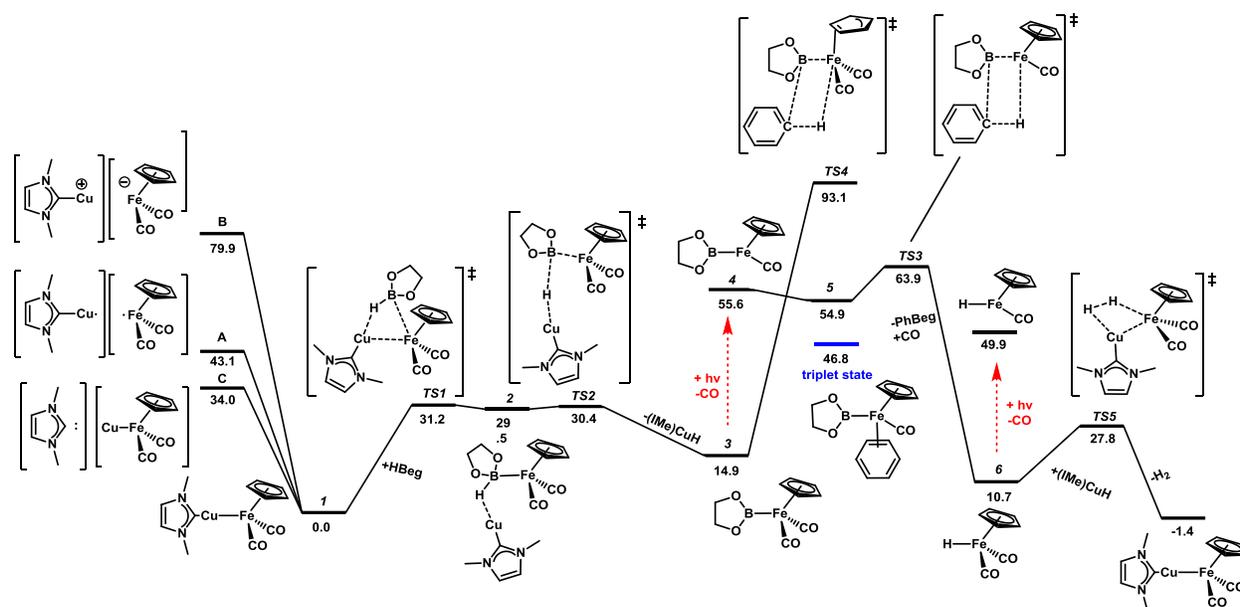
Figure 11. Full reaction mechanism for photochemical C-H borylation catalyzed using Cu-Fe cooperativity, including selected species determined not to be relevant to catalysis. Relative energies reference to **1** are shown in units of kcal/mol. Figure taken from Ref. **60**. Adapted with permission from (Parmelee, S. R.; Mazzacano, T. J.; Zhu, Y.; Mankad, N. P.; Keith, J. A. A Heterobimetallic Mechanism for C–H Borylation Elucidated from Experimental and Computational Data. *ACS Catal.* 5(6), 3689−3699 (2015)). Copyright (2015) American Chemical Society.

4.2.2 Nature of the catalyst in solution

The solution structure of (IPr)Cu-Fp was first considered before C−H borylation pathways, since this complex features an unsupported Cu−Fe bond that could potentially be labile due to its high degree of ionic character.[65]

In the solid state, (IPr)Cu-Fp has a short Cu−Fe distance (2.3462 Å).[65] There exists "semi-bridging" Cu···CO interactions for each CO unit within the Fp fragment. Intermolecular $C_{imidazole}$−H···O exists between the imidazole backbone C-H proton and the carbonyl oxygen atoms of the neighboring molecule. While the imidazole backbone engages in hydrogen bonding with solvent molecules in solution, the heterobimetallic catalysts do not aggregate significantly as they do in solid state. Nonetheless, solubility considerations indicated multiple scrambling pathways (e.g., Cu−Fe dissociation, NHC dissociation, bimolecular association).

The DFT-optimized structure of (IMe)Cu-Fp closely matched the experimentally determined structure of (IPr)CuFp,[65] featuring a short calculated Cu−Fe distance (2.349 Å) supported by two semibridging Cu···CO interactions. As shown in Figure 11, the neutral pair that would result from photochemical Cu−Fe bond homolysis, (IMe)Cu^0 + Fp (**A**), was calculated to be higher in energy than **1** by +43.1 kcal/mol. The dissociated ion pair that would result from Cu−Fe bond heterolysis, [(IMe)Cu]$^+$ [Fp]$^-$ (**B**), was calculated to be much higher in energy, +79.9 kcal/mol. The dissociation energy of the IMe ligand from (IMe)Cu-Fp (**C**) was calculated to be +34.0 kcal/mol. Collectively, these computational results indicate that either Cu−Fe bond dissociation or Cu-NHC dissociation are unlikely, as the calculated barriers are too high for these pathways to be accessible at room temperature.

4.2.3   B-H bimetallic oxidative addition

The heterobimetallic C−H borylation mechanism initiates with BOA of a B−H bond at the Cu−Fe core of (IPr)Cu-Fp.[9] This transformation can be regarded as the bimetallic analogue of the more traditional monometallic OA of a B−H bond at a single-site Ir catalyst.[56]

The overall B-H BOA reaction between **1** and H-Beg (Beg = B[κ^2- O(CH$_2$)$_2$O]) generates (IMe)Cu−H and Fp-Beg after a two-barrier process (Figure 11). The B−H bond of H-Beg was inserted into the Cu−Fe bond of **1** to generate complex **2** via a transition state, **TS1**. Intermediate **2** with thermodynamically uphill 29 kcal/mol compared to **1**, is essentially a tight ion pair with the formulation [(IMe)Cu][Fp(H-Beg)]. As shown in Figure 12, there exist attractive interactions between Cu and the boron H (1.62 Å) together with the glycolate O (2.41 Å). **TS1** appears to be a conventional ligand exchange mechanism, where the Fe−B bond is almost entirely formed (2.14 Å) while the Cu−Fe bond is substantially lengthened (3.29 Å). In addition, the B−H bond in complex **2** and **TS1** is ~1.38 Å while the B−H bond in HBeg is 1.19 Å. The increased B−H bond lengths shows that the B−H bond is partially activated with a Cu−H interaction occurring with an interatomic distance of ~1.61 Å.
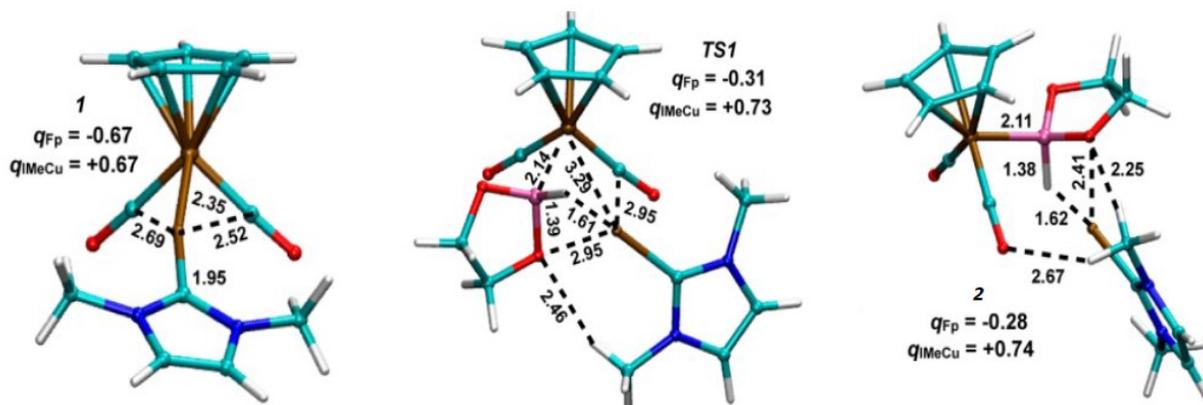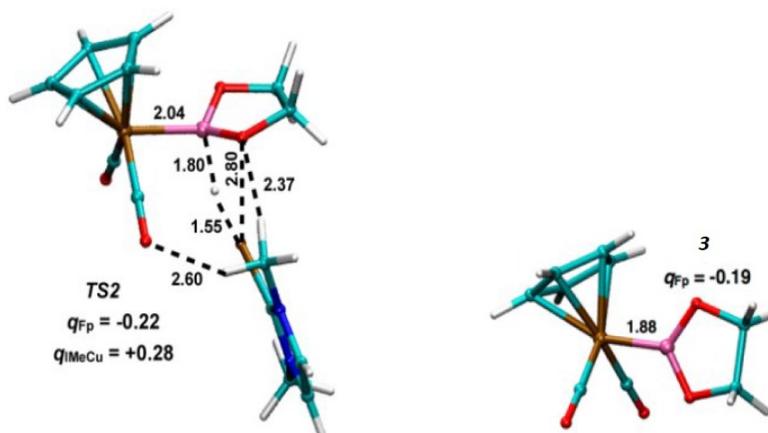
Figure 12. Reaction intermediates and transition states involved during B-H activation. Reported interatomic distances are given in Å. Figure taken from Ref. **60**. Adapted with permission from (Parmelee, S. R.; Mazzacano, T. J.; Zhu, Y.; Mankad, N. P.; Keith, J. A. A Heterobimetallic Mechanism for C−H Borylation Elucidated from Experimental and Computational Data. *ACS Catal.* 5(6), 3689−3699 (2015)). Copyright (2015) American Chemical Society.

Meanwhile, B−H bond is activated from complex **2** via **TS2** (see Figure 11). The activation barrier for B−H bond breaking is 1.4 kcal/mol relative to complex **2**. In **TS2**, the B−H bond lengthens significantly to 1.80 Å, while the Cu−H bond shortens to 1.55 Å simultaneously with the Cu···O−B bond lengthening to 2.80 Å. Complex **3** with the Fe−B bond fully formed (1.88 Å) is produced with +14.9 kcal/mol relative to **1**.

Notably, the relative energy difference between **TS1** and **TS2** is 0.8 kcal/mol and we cannot rule out that **TS2** may actually have higher energy, but our analysis shows that these energies are comparable.

4.2.4 Photochemical C-H borylation

Our computational results here supported that Cu cooperativity is not required for C−H borylation, which is mediated by the Fe fragment and requires UV irradiation[66]. CO is photochemically dissociated to generate an unsaturated, 16-electron Fe intermediate followed by C-H borylation and Fp−Bpin is the active borylating species during catalysis.

With the (IMe)CuH group no longer bound to the Fp, two newly formed (IMe)CuH species may dimerize in solution with a small energy increase of 1.6 kcal/mol. However, since the concentration of (IMe)CuH is expected to be low in this reaction, this small dimerization energy is not included in our reaction energies.

The reaction between Fp-Beg and benzene was calculated to be thermodynamically downhill by −4.2 kcal/mol to generate Fp-H and Ph-Beg. The CO dissociation energy from **3** to complex **4** was calculated to be 40.7 kcal/mol, consistent with high-energy UV irradiation requirement. Coordination of a solvent benzene molecule to the Fe intermediate is energetically downhill by −0.7 kcal/mol to form complex **5**. The fact that benzene binds much less strongly to the Fe than CO is likely the reason why neat arene substrates in the stoichiometric and catalytic C−H borylation reactions are required for this reaction. Without high concentrations of arenes, the CO would more rapidly recombine to the catalyst and block the vacant site needed to proceed in the reaction mechanism.

An iron hydride **6** and the borylation product are produced from the benzene substrate transferring to the Beg via **TS3**, a four-centered transition state. The barrier energy is only 9.0 kcal/mol relative to intermediate **5**. **TS3** has a broken C−H bond of benzene with a bond distance of 1.66 Å, compared to a value of 1.12 Å in complex **5** and 1.09 Å in the isolated benzene molecule. In **TS3**, the Fe−H bond is fully formed at a distance of 1.46 Å, and the Fe−B bond

length remains 1.98 Å over the course of transforming from **5** to **TS3**. B−C bond forms with interatomic interaction distance decreasing from 2.76 Å in **5**, to 2.12 Å in **TS3**, and finally to 1.55 Å in the final borylation product.

According to our calculation results, the triplet radical state of complex **5** is −8.1 kcal/mol lower in energy than its singlet state where the benzene molecule is coordinated to the Fp group. In the triplet state, the two unpaired electrons are located on the Fe center, and the benzene molecule no longer coordinates to but remains near the vacant bonding site. A triplet state seems thermodynamically accessible after CO loss. However, attempts at locating a triplet analog of **TS3** resulted in species with over 50 kcal/mol uphill relative to **TS3** and thus were not pursued further. Therefore, subsequent steps to form the B−C bond should proceed on the singlet state potential energy surface. If the reaction dynamics permit the triplet state to be accessible, the relative barrier of traversing **TS3** is still less than 20 kcal/mol and can be considered thermodynamically feasible at room temperature.

Another transition state **TS4** involves direct reaction between Fp-Beg and an outer-sphere benzene molecule. This transition state featured a ring-slipped η2-coordinated Cp, presumably to accommodate the additional benzene ligand at Fe. However, the energy of **TS4** is 20.0 kcal/mol higher relative to **TS3**. Thus, this pathway is considered to be unlikely even under UV irradiation conditions.
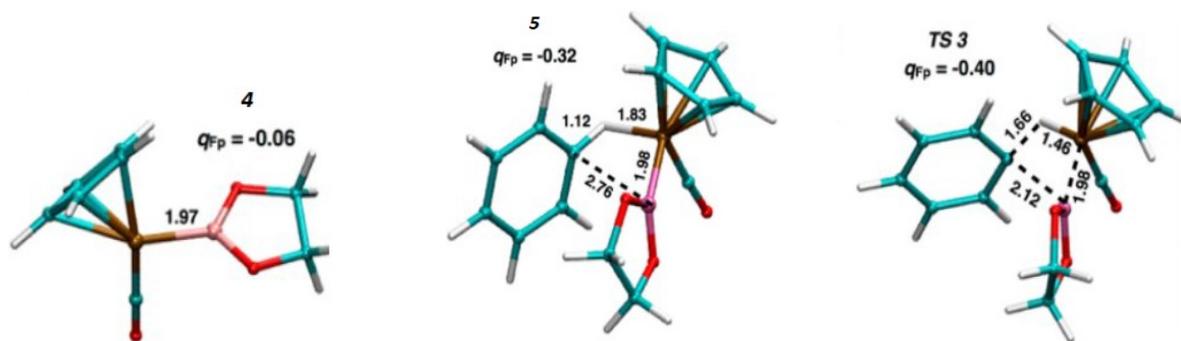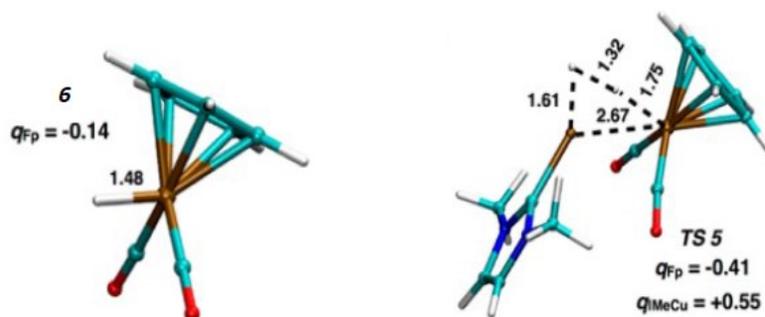
Figure 13: Reaction intermediates and transition states involved during borylation and H_2 evolution. Reported interatomic distances are given in Å. Figure taken from Ref. **60**. Adapted with permission from (Parmelee, S. R.; Mazzacano, T. J.; Zhu, Y.; Mankad, N. P.; Keith, J. A. A Heterobimetallic Mechanism for C–H Borylation Elucidated from Experimental and Computational Data. *ACS Catal.* 5(6), 3689−3699 (2015)). Copyright (2015) American Chemical Society.

4.2.5   H-H bimetallic reductive elimination

(IPr)Cu-Fp is regenerated and H_2 is liberated via BRE, a two-electron redox process (Figure 10c).[9] Loss of H_2 from **6** to regenerate **1** was calculated to be downhill by −12.1 kcal/mol. A concerted, four-centered transition state (**TS5**) was also located. The energy of **TS5** is +17.1 kcal/mol uphill relative to the energy of **6**. As shown in Figure 13, interatomic coordinates in this transition state are intermediate between those determined for the reactant **6** and the lone (IMe)CuH fragment (with a Cu−H bond distance of 1.51 Å). The Cu−Fe (2.67 Å) and H−H (1.32 Å) bonds are partially formed, and the Fe−H (1.75 Å) and Cu−H (1.61 Å) bonds are partially broken. An alternative pathway involving CO loss from Fp-H also was also investigated, but a fully optimized transition state was not found. Such a process is considered superfluous because we experimentally observe that the H−H BRE reaction does not require UV irradiation.

4.3   LIGAND SIZE EFFECT

Ligand size effects of the catalyst were also considered. We calculated the reaction energies of 1→2 using the full (IPr)Cu-Fp catalyst instead of the (IMe)Cu-Fp model catalyst. The relative energy with (IPr)Cu-Fp is 27.3 kcal/mol instead of 29 kcal/mol for (IMe)Cu-Fp. Since the 1.7 kcal/mol difference is within the margin of error for our DFT calculation, it cannot be interpreted as evidence that the larger ligands result in substantially lower reaction barriers. Additionally, the similarity in barrier heights indicate that (IMe)Cu-Fp is a reasonable model for catalysis occurring with (IPr)Cu-Fp.

4.4   AN ADDITIONAL BORANE OR COPPER MOLECULE

For more confirmation on the B-H BOA process, the pathway **1**→**TS1**→**2**→**TS2**→**3** with a second H-Beg molecule was considered. Relative to the energy of **1** with a second H-Beg complex, the second H-Beg slightly raises the relative energy of **TS1** by +0.9 kcal/mol, and modestly lowers the relative energy of **TS2** by −4.8 kcal/mol.

The possible influence of a second (IMe)CuH group on the BOA process was also considered. Additional Cu complex lowers the binding energy of complex **2** by −8.2 kcal/mol. **TS1** and **TS2** with the second (IMe)CuH group were not characterized. While our calculations support a lower energy pathway in the presence of additional stabilizing molecules, ternary reaction mechanisms typically bring a very high entropic barrier and thus are quite rare. Thus, they are assumed to be not relevant for this reaction. In principle, microkinetic modeling can be

carried out for a comparative study of how concentrations of borane and copper influence reaction rates, but this is out of the scope of the present work.

4.5   CONCLUSIONS AND FUTURE WORK

Overall, the entire borylation process is slightly exergonic, and UV irradiation is required for at least one reaction step. Fe−Cu bond breaking and B−H bond activation occur via two separate reaction steps to produce Fe−Beg. Since there is uncertainty in the energies for **TS1** and **TS2**, either **TS1** or **TS2** or a different process may be consistent with the experimentally expected barrier. UV irradiation allows a solvent benzene molecule to coordinate to the metal site after the removal of CO from Fp fragment. High concentrations of arenes might be required as solvent to bind intermediate **4** before it is recombined with CO. Subsequent C−H borylation occurs through singlet state energy surface, since reaction energies out of the triplet state are higher than energies needed to traverse **TS1** and **TS2**. At last, the catalyst (IPr)Cu-Fp is regenerated via a H−H bimetallic reductive elimination.

Our calculated results are not enough to definitely explain if photolysis of CO occurs from **3**, but the computational predictions support that overall barriers are lowest when photolysis occurs after B−H activation. To further improve this catalyst system, new designs should focus on better facilitating borane insertion into the Cu−Fe bond as well as lowering the barrier for B−H activation.

It was indicated that other OA/RE cycling at single-site precious metal can instead be carried out with earth-abundant bimetallic reaction centers. A platform was provided here from

which further studies on bimetallic organometallic complexes can be compared to canonical mechanisms involving one metal center.

SAMPLE CALCULATIONS

A.1   REACTION ENERGY OF HYDRIDE TRANSFER

Hydride transfer reaction:

$$Co(dmpe)_2H + CO_2 \rightarrow Co(dmpe)_2{}^+ + HCO_2{}^-$$
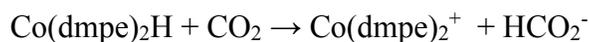
At T=298K:

A: $G_{298}(Co(dmpe)_2H)$ = -2023579.2 kcal/mol (after solvation)

B: $G_{298}(CO_2)$ = -118344.2 kcal/mol (after solvation)

C: $G_{298}(Co(dmpe)_2{}^+)$ = -2023148.6 kcal/mol (after solvation)

D: $G_{298}(HCO_2{}^-)$ = -118783.3 kcal/mol (after solvation)

E: $\Delta G_{acetonitrile}^*$ = **C + D − A −B** = -8.5 kcal/mol

Hydride energy calculation:

$$H_2 \rightarrow H^+ + H^-$$

At T=298K:

F: $G_{298}(H_2)$ = -735.5 kcal/mol (after solvation)

G: $G_{298}(H^+)$ = -264.6 kcal/mol (empirical after solvation)

H: $\Delta G^*_{acetonitrile}$ = 76 kcal/mol (empirical after solvation)

I: $G_{298}(H^-)$ = **F – G + H** = -394.9 kcal/mol (after solvation)

Hydride dissociation energy calculation:
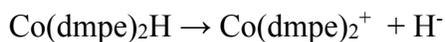
$$Co(dmpe)_2H \rightarrow Co(dmpe)_2^+ + H^-$$

At T=298K:

A: $G_{298}(Co(dmpe)_2H)$ = -2023579.2 kcal/mol(after solvation)

C: $G_{298}(Co(dmpe)_2^+)$ = -2023148.6 kcal/mol (after solvation)

I: $G_{298}(H^-)$ = F – G + H = -394.9 kcal/mol (empirical after solvation)

J: $\Delta G^*_{acetonitrile}$ = **C + I – A** = 35.7 kcal/mol

A.2   PKA CALCUALTION

pK_a calculation:
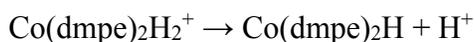
$$Co(dmpe)_2H_2^+ \rightarrow Co(dmpe)_2H + H^+$$

At T=298K:

A: $G_{298}(Co(dmpe)_2H)$ = -2023579.2 kcal/mol(after solvation)

G: $G_{298}(H^+)$ = -264.6 kcal/mol (empirical after solvation)

K: $G_{298}(cis\text{-}Co(dmpe)_2H_2^+)$ = -2023889.8 kcal/mol (after solvation)

L: $\Delta G^*_{acetonitrile}$ = **A+ G – K** = 46.0 kcal/mol

M: pK_a = **L** / (2.303* RT) = **<u>33.7</u>**

BIBLIOGRAPHY

1. Jeletic, M. S.; Mock, M. T.; Appel, A. M.; Linehan, J. C. A Cobalt-Based Catalyst for the Hydrogenation of CO_2 under Ambient Conditions. *J. Am. Chem. Soc*. **135**, 11533-11536 (2013).

2. Haxel, G. B.; Boore, S.; Mayfield, S. from USGS. http://pubs.usgs.gov/fs/2002/fs087-02/ (2002).

3. Jessop, P. G.; Ikariya, T.; Noyori, R. Homogeneous Hydrogenation of Carbon Dioxide. *Chem. Rev.* **95**, 259-272 (1995).

4. Tanaka, R.; Yamashita, M.; Nozaki, K. Catalytic Hydrogenation of Carbon Dioxide Using Ir(III)-Pincer Complexes. *J. Am. Chem. Soc.* **131**, 14168-14169 (2009).

5. Qi, X.-J.; Liu, L.; Fu, Y.; Guo, Q.-X. *Ab Initio* Calculations of pK_a Values of Transition-Metal Hydrides in Acetonitrile. *Organometallics* **25**(25), 5879-5886 (2006).

6. Qi, X.-J.; Fu, Y.; Liu, L.; Guo, Q.-X. Ab Initio Calculations of Thermodynamic Hydricities of Transition-Metal Hydrides in Acetonitrile. *Organometallics* **26**(17), 4197-4203 (2007).

7. Angermund, K.; Baumann, W.; Dinjus, E.; Fornika, R.; Görls, H.; Kessler, M.; Krüger, C.; Leitner, W.; Lutz, F. Complexes [(P_2)Rh(hfacac)] as Model Compounds for the Fragment [(P_2)Rh] and as Highly Active Catalysts for CO_2 Hydrogenation: The Accessible Molecular Surface (AMS) Model as an Approach to Quantifying the Intrinsic Steric Properties of Chelating Ligands in Homogeneous Catalysis. *Chem.-Eur. J.* **3**, 755 (1997).

8. Peppernick, S. J.; Dasitha Gunaratne, K. D.; Castleman, A. W., Jr. Superatom Spectroscopy and the Electronic State Correlation between Elements and Isoelectronic Molecular Counterparts. *Proc. Natl. Acad. Sci. U. S. A.* **107**, 975−980 (2010).

9. Mazzacano, T. J.; Mankad, N. P. Base Metal Catalysts for Photochemical C-H Borylation That Utilize Metal-Metal Cooperativity. *J. Am. Chem. Soc.* 135(46), 17258−17261 (2013).

10. Hohenberg, P.; Kohn, W. Inhomogeneous Electron Gas. *Phys. Rev.* **136**, B864 (1964).

11. Kohn, W.; Sham, L. J. Self-Consistent Equations Including Exchange and Correction Effects. *Phys. Rev.* **140**, A1133 (1965).

12. Sun, J.; Perdew, J. P.; Ruzsinszky, A. Semilocal Density Functional Obeying a Strongly Tightened Bound for Exchange. *Proc. Natl. Acad. Sci. U. S. A.* **112**, 685-689 (2015).

13. Ceperley, D. M.; Alder, B. Ground State of the Electron Gas by a Stochastic Method. *J. Phys. Rev. Lett.* **45**, 566 (1980).

14. Vosko, S. H.; Wilk, L.; Nusair, M. Accurate Spin-Dependent Electron Liquid Correlation Energies for Local Spin Density Calculations: A Critical Analysis. *Can. J. Phys.* **58**, 1200 (1980).

15. Perdew, J. P.; Wang, Y. Pair-Distribution Function and Its Coupling-Constant Average for the Spin-Polarized Electron Gas. *Phys. Rev. B* **45**, 13244 (1992).

16. Perdew, J. P.; Chevary, J. A.; Vosko, S. H.; Jackson, K. A.; Pederson, M. R.; Singh, D. J.; Fiolhais, C. Atoms, Molecules, Solids, and Surfaces: Applications of the Generalized Gradient Approximation for Exchange and Correlation. *Phys. Rev.* B **46**, 6671 (1992).

17. Becke, A. D. Density-Functional Exchange-Energy Approximation with Correct Asymptotic Behavior. *Phys. Rev.* A **48**, 3098 (1988).

18. Lee, C.; Yang, W.; Parr, R. G. Development of the Colle-Salvetti Correlation-Energy Formula into a Functional of the Electron Density, *Phys. Rev.* B **37**, 785 (1988).

19. Perdew, J. P. Density-Functional Approximation for the Correlation Energy of the Inhomogeneous Electron Gas. *Phys. Rev.* B **33**, 8822 (1986); Erratum *Phys. Rev.* B **34**, 7406 (1986).

20. aShevlin, S. A.; Guo, Z. X. Density Functional Theory Simulations of Complex Hydride and Carbon-Based Hydrogen Storage Material. *Chem. Soc. Rev.* **38**, 211-225 (2009).

21. Kim, K.; Jordan, K. D. Comparison of Density Functional and MP2 Calculations on the Water Monomer and Dimer. *J. Phys. Chem.* **98**(40), 10089-10094 (1994).

22. Cramer, C. J. *Essentials of Computational Chemistry*. Chichester: John Wiley & Sons, Ltd. 191-232 (2002).

23. Čížek, J. On the Correlation Problem in Atomic and Molecular Systems. Calculation of Wavefunction Components in Ursell-Type Expansion Using Quantum-Field Theoretical Methods. *J. Chem. Phys.* **45**, 4256 (1966).

24. Szabo, A.; Ostlund, N. S. *Modern Quantum Chemistry: Introduction to Advanced Electronic Structure Theory*. McGraw-Hill, Inc., NJ (1989).

25. Riplinger, C.; Neese, F. An Efficient and Near Linear Scaling Pair Natural Orbital Based Local Coupled Cluster Method. *J. Chem. Phys.* **138**, 034106 (2013).

26. Riplinger, C.; Sandhoefer, B.; Hansen, A.; Neese, F. Natural Triple Excitations in Local Coupled Cluster Calculations with Pair Natural Orbitals. *J. Chem. Phys.* **139**, 134101 (2013).

27. Marenich, A. V.; Cramer, C. J.; Truhlar, D. G. Universal Solvation Model Based on Solute Electron Density and on a Continuum Model of the Solvent Defined by the Bulk Dielectric Constant and Atomic Surface Tensions. *J. Phys. Chem. B* **113**(18), 6378-6396, (2009).

28. Klamt, A.; Schüürmann, G. COSMO: a New Approach to Dielectric Screening in Solvents with Explicit Expressions for the Screening Energy and Its Gradient. *J. Chem. Soc., Perkin Trans. 2* 799-805, (1993).

29. Truong, T. N.; Stefanovich, E. V. Analytical First and Second Energy Derivatives of the Generalized Conductorlike Screening Model for Free Energy of Solvation. *J. Chem. Phys.* **103**, 3709 (1995).

30. Mantina, M.; Chamberlin, A. C.; Valero, R.; Cramer, C. J.; Truhlar, D. G. Consistent van der Waals Radii for the Whole Main Group. *J. Phys. Chem. A* **113**(19), 5806-5812 (2009).

31. Sierka, M.; Hogekamp, A.; Ahlrichs, R. Fast Evaluation of the Coulomb Potential for Electron Densities Using Multipole Accelerated Resolution of Identity Approximation. *J. Chem. Phys.* **118**, 9136–9148 (2003).

32. Schäfer, A.; Horn, H.; Ahlrichs, R. Fully Optimized Contracted Gaussian basis sets for atoms Li to Kr. *J. Chem. Phys.* **97**, 2571 (1992).

33. Grimme, S.; Antony, J.; Ehrlich, S.; Krieg, H. A Consistent and Accurate Ab Initio Parametrization of Density Functional Dispersion Correction (DFT-D) for the 94 elements H-Pu. *J. Chem. Phys.* **132**, 154104-1−154104-19 (2010).

34. Keith, J. A.; Cater, E. A. Quantum Chemical Benchmarking, Validation, and Prediction of Acidity Constants for Substituted Pyridinium Ions ans Pyridinyl Radicals. *J. Chem. Theory Comput.* **8**(9), 3187-3206 (2012).

35. Ho, J.; Coote, M. L. A Universal Approach for Continuum Solvent pK_a calculations: are we there yet? *Theor. Chem. Acc.* **125**, 3-21 (2009).

36. McQuarrie, D. A. *Statistical Mechanics.* 1st ed.; University Science Books: Sausalito, 86 (2000).

37. Marenich, A. V.; Ho, J.; Coote, M. L.; Cramer, C. J.; Truhlar, D. G. Computational Electrochemistry: Prediction of Liquid-Phase Reduction Potentials. *Phys. Chem. Chem. Phys.* **16**, 15068-15106 (2014).

38. Kelly, C. P.; Cramer, C. J.; Truhlar, D. G. Single-Ion Solvation Free Energies and the Normal Hydrogen Electrode Potential in Methanol, Acetonitrile, and Dimethyl Sulfoxide. *J. Phys. Chem. B* **111**(2), 408-422 (2007).

39. Tissandier, M. D.; Cowen, K. A.; Feng, W. Y.; Gundlach, E.; Cohen, M. H.; Earhart, A. D.; Coe, J. V.; Tuttle, T. R. The Proton's Absolute Aqueous Enthalpy and Gibbs Free Energy of Solvation from Cluster-Ion Solvation Data. *J. Phys. Chem. A* **102**, 7787−7794 (1998).

40. Cook, T. R.; Dogutan, D. K.; Reece, S. Y.; Surendranath, Y.; Teets, T. S.; Nocera, D. G. Solar Energy Supply and Storage for the Legacy and Nonlegacy Worlds. *Chem. Rev.* **110**, 6474 (2010).

41. Whitney, S. M.; Houtz, R. L.; Alonso, H. Advancing Our Understanding and Capacity to Engineer Nature's CO_2-Sequestering Enzyme, Rubisco. *Plant Physiology* **155**, 27-35 (2011).

42. Walter, M. G.; Warren, E. L.; McKone, J. R.; Boettcher, S. W.; Mi, Q.; Santori, E. A.; Lewis, N. S. Solar Water Splitting Cells. *Chem. Rev.* **110**, 6446-6473 (2010).

43. DuBois, D. L.; Berning, D. E. Hydricity of Transition-Metal Hydrides and its role in CO2 reduction. *Appl. Organometal. Chem.* **14**, 860-862 (2000).

44. Curtis, C. J.; Miedaner, A.; Ellis, W. W.; DuBois, D. L. Measurement of the Hydride Donor Abilities of $[HM(diphosphine)_2]^+$ Complexes (M = Ni, Pt) by Heterolytic Activation of Hydrogen. *J. Am. Chem. Soc.* **124**, 1918 (2002).

45. Ciancanelli, R.; Noll, B. C.; DuBois, D. L.; DuBois, M. R. Comprehensive Thermodynamic Characterization of the Metal-Hydrogen Bond in a Series of Cobalt-Hydride Complexes. *J. Am. Chem. Soc.* **124**, 2984-2992 (2002).

46. TURBOMOLE, V6.5; University of Karlsruhe and Forschungszentrum Karlsruhe GmbH: Karlsruhe, Germany, 1989−2007; TURBOMOLE GmbH: Karlsruhe, Germany, 2007. Available from http://www.turbomole.com.

47. Weigend, F.; Ahlrichs, R. Balanced Basis Sets of Split Valence, Triple Zeta Valence and Quadruple Zeta Valence Quality for H to Rn: Design and Assessment of Accuracy. *Phys. Chem. Chem. Phys.* **7**, 3297 (2005).

48. Zheng, J.; Xu, X.; Truhlar, D. G. Minimally Augmented Karlsruhe Basis Sets. *Theor. Chem. Acc.* **128**, 295 (2011).

49. Neese, F. The ORCA Program System. *Wiley Interdiscip. Rev.: Comput. Mol. Sci.* **2**, 73 (2012).

50. Truhlar, D. G. Basis-Set Extrapolation. *Chem. Phys. Lett.* **294**, 45 (1998).

51. van Lenthe, E.; Baerends, E. J.; Snijders, J. G. Relativistic Total Energy Using Regular Approximations. *J. Chem. Phys.* **101**, 9783 (1994).

52. van Lenthe, E.; Snijders, J. G.; Baerends, E. J. The Zero-Order Regular Approximation for Relativistic Effects: The Effect of Spin-Orbit Coupling in Closed Shell Molecules. *J. Chem. Phys.* **105**, 6505 (1996).

53. Pliego, J. R., Jr.; Riveros, J. M. The Cluster−Continuum Model for the Calculation of the Solvation Free Energy of Ionic Species. *J. Phys. Chem. A* **105**(30), 7241-7247 (2001).

54. Sohn, S. S.; Bode, J. W. Catalytic Generation of Activated Carboxylates from Enals: A Product-Determining Role for the Base. *Organic Letters* **7**, 3873-3876 (2005).

55. Shiflett, M. B.; Yokozeki, A. Phase Behavior of Carbon Dioxide in Ionic Liquids: [Emim][Acetate], [Emim][Trifluoroacetate], and [Emim][Acetate]+[Emim][Trifluoroacetate] Mixtures. *J. Chem. Eng. Data* **54**, 108-114 (2009).

56. Mkhalid, I. A. I.; Barnard, J. H.; Marder, T. B.; Murphy, J. M.; Hartwig, J. F. C-H Activation for the Construction of C-B Bonds. *Chem. Rev.* **110**, 890−931 (2010).

57. Radlauer, M. R.; Day, M. W.; Agapie, T. Bimetallic Effects on Ethylene Polymerization in the Presence of Amines: Inhibition of the Deactivation by Lewis Bases. *J. Am. Chem. Soc.* **134**, 1478−1481 (2012).

58. Matsunaga, S.; Shibasaki, M. Recent Advances in Cooperative Bimetallic Asymmetric Catalysis: Dinuclear Schiff Base Complexes. *Chem. Commun.* **50**, 1044−1057 (2014).

59. Heyduk, A. F.; Nocera, D. G. Hydrogen Produced from Hydrohalic Acid Solutions by a Two-Electron Mixed-Valence Photocatalyst. *Science* **293**, 1639−1641 (2001).

60. Parmelee, S. R.; Mazzacano, T. J.; Zhu, Y.; Mankad, N. P.; Keith, J. A. A Heterobimetallic Mechanism for C–H Borylation Elucidated from Experimental and Computational Data. *ACS Catal.* **5**(6), 3689−3699 (2015).

61. Gordon, M. S.; Schmidt, M. W. *Advances in electronic structure theory: GAMESS a decade later. In Theory and Applications of Computational Chemistry: The First Forty Years*; Dykstra, C., Frenking, G., Kim, K., Scuseria, G., Eds.; Elsevier Science: Amsterdam, 1167−1189 (2005).

62. Hay, P. J.; Wadt, W. R. *Ab Initio* Effective Core Potentials for Molecular Calculations. Potentials for K to Au Including the Outermost Core Orbitals *J. Chem. Phys.* **82**, 270−283 (1985).

63. Cramer, C. J. *Essentials of Computational Chemistry: Theories and Models*, 2nd ed.; John Wiley & Sons, Inc.: Hoboken, NJ (2004).

64. Lynch, B. J.; Zhao, Y.; Truhlar, D. G. Effectiveness of Diffuse Basis Functions for Calculating Relative Energies by Density Functional Theory. *J. Phys. Chem. A* **107**, 1384−1388 (2003).

65. Jayarathne, U.; Mazzacano, T. J.; Bagherzadeh, S.; Mankad, N. P. Heterobimetallic Complexes with Polar, Unsupported Cu–Fe and Zn–Fe Bonds Stabilized by N-Heterocyclic Carbenes. *Organometallics* **32**, 3986−3992 (2013).

66. Waltz, K. M.; He, X.; Muhoro, C.; Hartwig, J. F. Hydrocarbon Functionalization by Transition Metal Boryls. *J. Am. Chem. Soc.* **117**, 11357−11358 (1995).